

Karpuk Aircraft

KR-1

Multi-Mission Amphibian



Response to 2016/2017 AIAA Foundation Graduate Individual Aircraft Design Competition Presented by
Embry-Riddle Aeronautical University (Daytona Beach)

Department of Aerospace Engineering



Karpuk Aircraft



Stanislav Karpuk

Design Engineer

AIAA account number: 511739

E-mail: karpuks@my.erau.edu

A handwritten signature in black ink, appearing to read "Karpuk", with a horizontal line extending to the right.

Advisor: Dr Snorri Gudmundsson

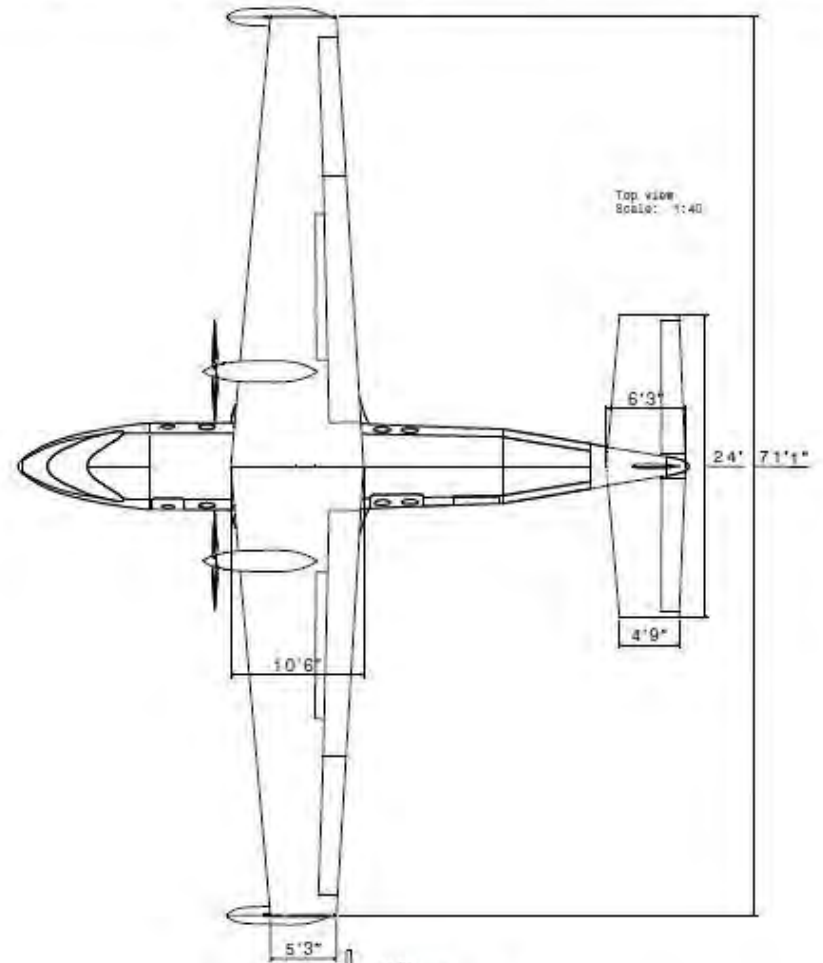
Executive Summary

Karpuk Aircraft would like to present a response to the request for proposal (RFP) provided by the American Institute of Aeronautics and Astronautics (AIAA) for 2016-2017 year. Due to potential benefits of amphibious passenger and cargo aircraft for regional aviation with limited resources to create airports and lack of existent aircraft designed for the presented requirements, the Company was asked to design an aircraft capable of carrying between 20 and 49 passengers or 5000lb of payload at the cruise speed no less than 200 knots. The aircraft shall be able to complete both VFR and IFR flights and complete four different missions. According to the first mission, the aircraft must fly 259nmi with 20 passengers and be able to take-off within 1500ft over a 50ft obstacle to a runway with dry pavement at Sea Level (SL) and 5000ft altitude with air temperature of +18⁰F at SL. The second mission is similar to the first, but the take-off is performed from water and the take-off distance shall not exceed 1900ft over a 50ft obstacle. The third mission requires the aircraft to complete a 1000ft flight with maximum amount of passengers, and the last one asks the aircraft to demonstrate a 500nmi flight with 5000lb cargo and be prepared for the next flight within 60 minutes. The aircraft shall be capable of taking off and landing from different quality of runways as well as fresh and salt water. In addition, the aircraft must demonstrate 20% reduction in fuel burn per passenger comparing to existing aircraft for a similar range. The aircraft will be certified with FAA 14 CFR Part 25, and the passenger model shall enter into the service in 2027. The KR-1 designed by Karpuk Aircraft is a conventional top-wing twin-turboprop aircraft featuring conventional tail for Short take-off and landing (STOL)

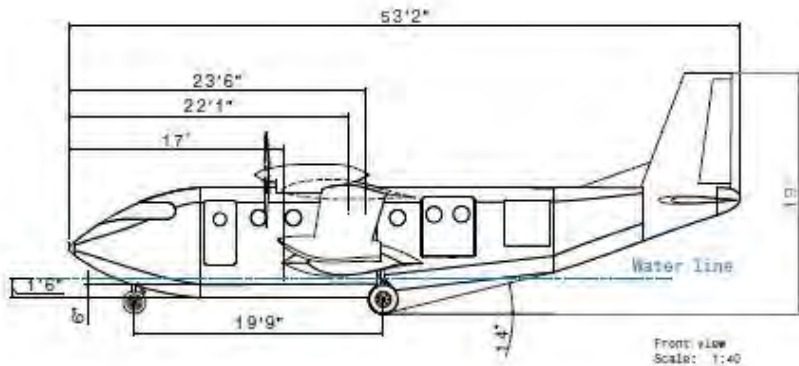
Wing Span (ft)	71
AR	9
Length (ft)	53.17
Height (ft)	19
Wing Loading	38
Taper Ratio	0.5
MAC length (ft)	8.18



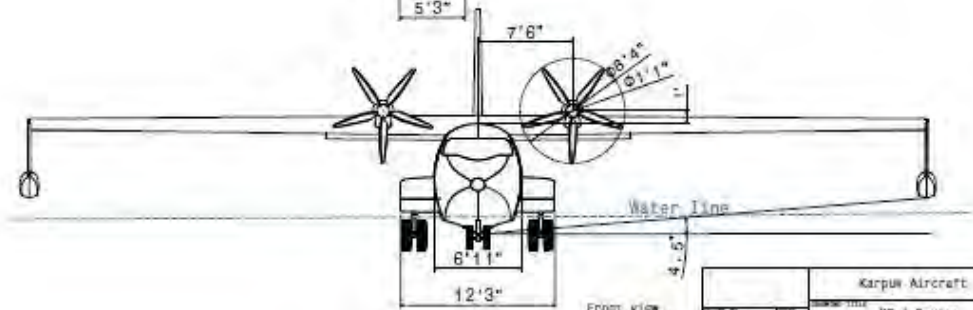
Isometric view
Scale: 1:40



Top view
Scale: 1:40



Front view
Scale: 1:40



Front view
Scale: 1:40

Karpus Aircraft	
Project No.	KR-1 S-view
Author	AS
Date	05.1.1
Scale	1:40

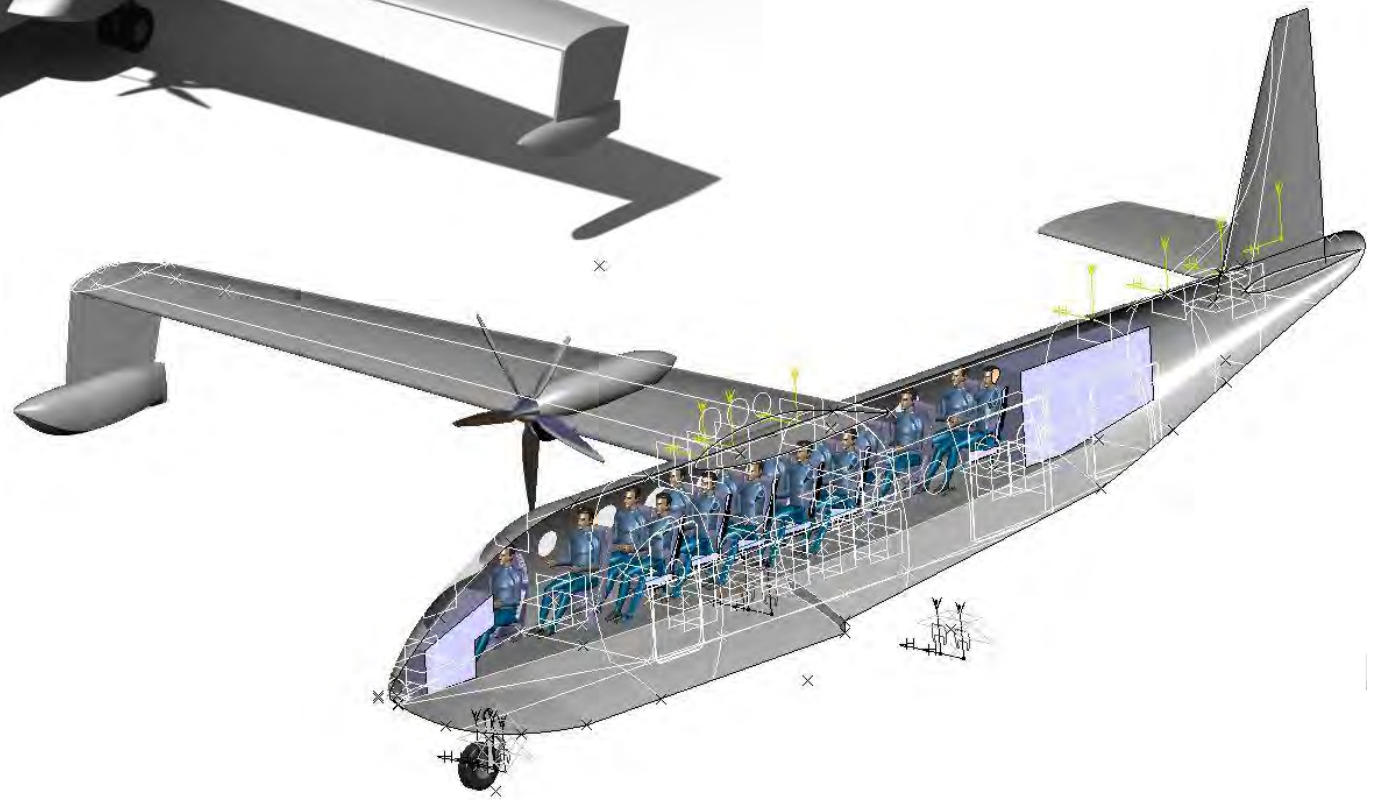


Table of Contents

List of Figures	7
Index of tables	10
1. Introduction	12
1.1. Mission Analysis.....	12
1.2. Competition study	13
2. Concept selection and Initial sizing	15
2.1. Aircraft Concept Trade study.....	15
2.2 Design Sizing and layout	19
3. Aerodynamic Design and analysis	20
3.1. Airfoil Selection.....	20
3.2. Wing configuration Design.....	22
3.3. Lift analysis.....	22
3.4. Drag analysis.....	25
3.5. High-Lift Devices	28
3.6. Aerodynamic performance.....	29
4. Propulsion	30
4.1. Engine selection	30
4.2. Propeller analysis and thrust estimation.....	31
4.3. Engine Placement.....	33
5. Weights	34
5.1. Weight Estimations.....	34
5.2. Center of Gravity	36
6. Hull and floats design	37
6.1. Hull shape Design	37
6.2. Floats design	42
7. Aircraft performance	43
7.1. Take-off and Landing	43
7.1.1. Ground take-off and landing	44
7.1.2. Water take-off and landing	47
7.2 Climb	50

7.3. Cruise	50
7.4. Steady-state turn.....	52
7.5. Descent.....	53
8. Structures.....	53
8.1. V-n Diagram	53
8.2. Material selection.....	54
8.3. Wing and tail structure.....	55
9. Stability and Control	60
9.1. Static stability and control analysis.....	60
10. Aircraft systems and layout.....	66
10.1. Landing gear	66
10.2. Cabin pressurization and air conditioning.....	69
10.3. Fuel system	69
10.4. Fuselage layout	69
10.5. Anti-icing system	72
11. Cost analysis	73
11.1 Fuel economy.....	73
11.2 Research, Development, Testing, and Evaluation	74
11.3. Operational Costs.....	75
12. Compliance Matrix	76
13. Conclusion	76
References.....	77

List of Figures

Figure 1.1.1: Mission profile for a 1000nm passenger mission.....	13
Figure 2.1.1: Concept 1 model.....	15
Figure 2.1.2: Concept 2 model.....	16
Figure 2.1.3. Concept 3 model.....	16
Figure 2.1.4. Concept 4 model.....	17
Figure 2.1.5. Weights for different strut configurations.....	18
Figure 2.1.6. CD for different strut.....	18
Figure 2.1.7. Fuel-to-Weight ratios for different strut configurations.....	19
Figure 2.2.1. Constraint diagram.....	19
Figure 3.1.1. NACA 65(2)-415 airfoil geometry.....	22
Figure 3.2.1. Wing layout.....	22
Figure 3.3.1. KR-1 VSP model.....	24
Figure 3.3.2. Lift coefficient comparison.....	24
Figure 3.3.3. Lift distribution at maximum AOA from OpenVSP.....	24
Figure 3.4.1. NACA65(2)-415 O-grid.....	26
Figure 3.4.2. Solution residuals.....	26
Figure 3.4.3. Airfoil pressure.....	26
Figure 3.4.1. Parasitic drag build-up at cruise speed.....	27
Figure 3.5.1. Lift coefficient for different configurations.....	28
Figure 3.5.2. Drag coefficient for different configurations.....	29
Figure 3.6.1 Lift-to-drag ratio for different aircraft configurations.....	30
Figure 4.1.1. Pratt & Whitney Canada PT6A-67B.....	31
Figure 4.2.1. Thrust output at different altitudes.....	32
Figure 4.2.2. Efficiency at different altitudes.....	32
Figure 4.3.1. Engine layout and propeller dimensions.....	33
Figure 5.1.1. Weight breakdown comparison using different methods.....	35
Figure 5.2.1. Load and balance diagram for Take-off, Landing, and Cruise.....	36
Figure 6.1.1. Hull nomenclature and common dimensions.....	37
Figure 6.1.2. Front view and hull dimensions.....	38

Figure 6.1.3 Side view and hull dimensions.....	39
Figure 6.1.4. Hull load factor vs stall speeds at different deadrise angles for landing configuration.....	40
Figure 6.1.5. Weight coefficient relation.....	41
Figure 6.1.6. Afterbody deadrise angle relation.....	41
Figure 6.1.7. Sternpost angle relation at step depths.....	41
Figure 6.1.8. Aftbody-to-beam ratio based on step depth.....	42
Figure 6.2.1. Float volume and water clearance vs float location.....	42
Figure 6.2.2. Float layout and dimensions.....	43
Figure 7.1.1. Take-off run for for the 250nmi STOL mission with 20 passenger at sea level.....	45
Figure 7.1.2. Water hull resistance estimation.....	47
Figure 7.1.3. Trim angle estimation.....	47
Figure 7.2.1. Climb performance for a 1000nmi mission weight with full payload.....	50
Figure 7.3.1. Flight Envelope.....	51
Figure 7.3.2. Payload Range Curve.....	51
Figure 7.4.1. Turn Performance Map.....	52
Figure 7.4.1. Descent Performance Diagram.....	53
Figure 8.1.1. V-n Diagram at cruise altitude.....	54
Figure 8.3.1. Wing coordinate system used for structural analysis.....	55
Figure 8.3.2. Internal forces and moments experienced by the wing. V=215KTAS, H=16500ft, n=3.....	56
Figure 8.3.3. Internal forces and moments experienced by the H-tail. V=215KTAS, H=16500ft, n=3.....	56
Figure 8.3.4. Internal forces and moments experienced by the H-tail. V=215KTAS, H=16500ft, n=3.....	57
Figure 8.3.5. Wing Front and rear spar dimensions.....	58
Figure 8.3.6. Horizontal tail Front and rear spar dimensions.....	59
Figure 8.3.7. Vertical Front and rear spar dimensions.....	59
Figure 8.3.8. Wing structural layout.....	59
Figure 8.3.9. Empennage structural layout.....	59
Figure 8.3.10. Shear and Moment diagrams of the fuselage.....	60
Figure 8.3.11. Stringers layout.....	60
Figure 9.1.1. Horizontal tail layout.....	61
Figure 9.1.2. Horizontal tail vertical location diagram.....	61
Figure 9.1.3. Engine-out case free-body diagram	62

Figure 9.1.4. Vertical tail layout.....	62
Figure 9.1.5. Wake blockage diagram.....	63
Figure 9.1.6. Aileron layout.....	63
Figure 9.2.1. Longitudinal motion poles and zeros.....	64
Figure 9.2.2. Lateral motion poles and zeros.....	64
Figure 10.1.1. Longitudinal landing gear location.....	66
Figure 10.1.2. Lateral landing gear location.....	67
Figure 10.1.3. Landing gear retraction.....	68
Figure 10.1.3. Landing gear layout.....	69
Figure 10.3.1. Fuel tank layout.....	70
Figure 10.4.1. Cabin top view.....	70
Figure 10.4.2. Cabin front view	71
Figure 10.4.3. Seat pitch.....	71
Figure 10.4.4. Doors dimensions.....	71
Figure 10.4.5. KR-1 cargo configuration.....	71
Figure 10.4.6. Baggage compartment side view.....	72
Figure 10.4.7. Cockpit view.....	72
Figure 10.5.1. Anti-icing cross-section.....	72
Figure 10.5.2. Anti-icing system layout.....	72
Figure 11.2.1. RTD&E Cost breakdown.....	74
Figure 11.2.2. Production breakeven point (Eastlake Model)	75
Figure 11.3.1. Operational cost breakdown.....	75

Index of tables

Table 1.2.1. Competitor aircraft parameters.....	14
Table 2.1.1. Trade study.....	17
Table 3.1.1. Airfoil characteristics of best selected airfoils at $Re=9$ million.....	21
Table 3.1.2. Scoring analysis of the airfoils.....	21
Table 3.2.1. Wing geometric parameters.....	23
Table 3.3.1. Comparison of stall behavior.....	24
Table 3.4.1. Critical boundary layer locations with respect to the chord.....	26
Table 3.4.2. Parasitic drag build-up at cruise speed.....	27
Table 3.5.1. Geometric layout and of flaps, slats, and spoilers.....	28
Table 3.5.2. CL_{max} for various configurations.....	29
Table 4.4.1. Pratt & Whitney Canada PT6A-PT6A-68C data.....	31
Table 4.2.1. Maximum tip Mach number for main flight altitudes.....	32
Table 5.1.1. General weight data.....	34
Table 5.1.2. Empty-weight breakdown.....	35
Table 5.2.1. CG comparison between Sdraey and KR-1.....	36
Table 6.1.1. Sea State 3 requirements and maximum wave height for KR-1.....	42
Table 7.1.1. FAR Part 25 speed requirements and values.....	44
Table 7.1.2. Ground take-off distance data for different mission cases at sea level.....	45
Table 7.1.3. Ground take-off distance data for different mission cases at 5000ft.	46
Table 7.1.4. Ground landing distance data for different mission cases at sea level.....	46
Table 7.1.5. Ground landing distance data for different mission cases at 5000ft.....	47
Table 7.1.6. Water take-off distance data for different mission cases at sea level and 5000ft.....	49
Table 7.1.7. Water landing distance data for different mission cases at sea level.....	49
Table 7.1.8 Water landing distance data for different mission cases at 5000ft.....	49
Table 7.3.1. Payload, Range, and Range for critical points of the Payload Range Curve.....	52
Table 8.2.1. Aluminum 2024-T4 material properties.....	54
Table 9.1.1. Horizontal tail parameters.....	61
Table 9.1.2. Vertical tail parameters.....	63

Table 9.1.3. Roll rate requirements comparison.....	63
Table 9.1.5. Static stability coefficients.....	64
Table 9.2.1. Dynamic stability analysis of KR-1.....	65
Table 10.1.1. Percent MTOW experienced by the nose landing gear at cg limits.....	66
Table 10.1.2. Tires specs used for KR-1 landing gear.....	68
Table 11.1.1. Fuel economy comparison	73
Table 11.2.1. Rates for aircraft development	74

1. Introduction

1.1. Mission Analysis

Current RFP provided by AIAA requires designing a Multi-Mission Amphibious (MMA) aircraft capable of carrying at least 20 and no more than 49 passengers. The aircraft shall be able to complete IFR and VFR mission, have a range of 1000nmi with maximum passenger density. Cruise speed of the aircraft must be greater than 200 knots with more than 250 knots desired. The aircraft must demonstrate at least 20% reduction in fuel burn per passenger comparing to existing aircraft for a similar mission range (200nmi). Minimum seat pitch of 28 in must be satisfied and minimum baggage volume for each passenger shall not be less than 4 cubic feet.

The aircraft shall be able to demonstrate a variety of take-off capabilities. Take-off and landing can be performed from dirt, grass, metal mat, gravel, asphalt, etc. Water take-off and landing capability must include both fresh and salt water. In addition, STOL capabilities must be satisfied: the aircraft loaded with 20 passengers for the range of 250nmi shall take-off and land within 1500ft on a dry pavement and within 1900ft on water.

Cargo mission requires the aircraft to carry 5000 lb of payload for a 500 nmi mission. The aircraft shall be able to be prepared for the next flight within 60 minutes (unload, refuel, and load cargo) and is desired to have an ability to carry odd shaped cargo or a standard container.

Existing or coming to service by 2027 engines must be considered for the current aircraft design.

The crew must consist of two pilots and one cabin crew member.

Anti-icing system must be installed on the aircraft to prevent icing.

The aircraft will be certified with FAA 14 CFR Part 25, and the passenger version should enter the service by 2027.

The mission profile is common for all mission except for the flight range. Figure 1.1.1 presents the longest IFR mission with maximum density of passengers.

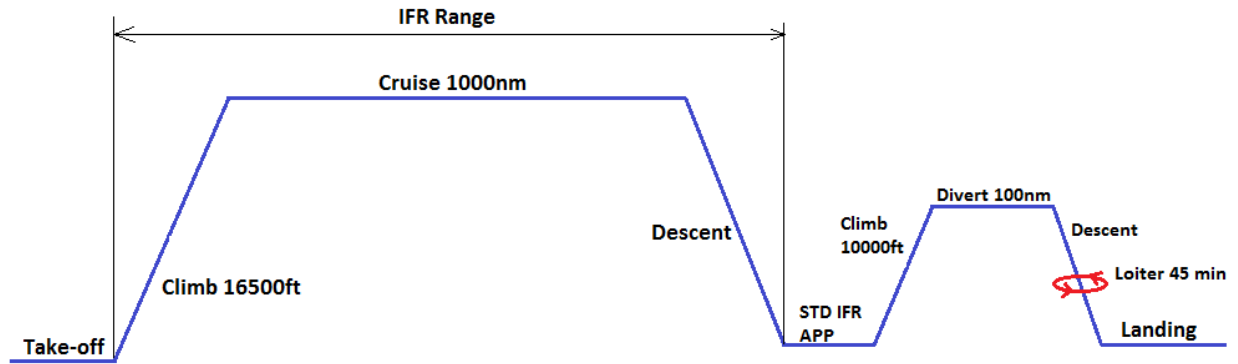


Figure 1.1.1. IFR Mission profile for a 1000nm passenger mission

Several challenges can be observed from the mission requirements. The first one deals with short take-off and landing requirements that will put significant constraints on engine selection and configuration selection. High-lift devices study will play an important role in achieving the requirements as well. In addition, fuel consumption forces the configuration to demonstrate significant efficiency improvement to satisfy the requirements. Finally, short-time preparation for a cargo flight requires wise configuration and layout solution to satisfy the task.

1.2. Competition study

A number of similar aircraft were studied to investigate common geometric and performance parameters. Amphibious aircraft with passenger capacity of more than 18 passengers were considered for the competition. Three aircraft were chosen: DHC-6 Twin Otter Series 400 [1], Grumman G-73 Mallard [1], and Beriev Be-112 [2] concept. Table 1.1.1 shows aircraft properties of the competitors. Based on the comparison study, common aspect ratio of the aircraft ranges from eight to ten, service ceiling is close to 25000ft, and power-to-weight ratio lies between 0.086 and 0.12. However, other parameter such as gross weight and wing loading vary substantially.

			
Aircraft name	DHC-6 Twin Otter Series 400	Grumman G-73 Mallard	Beriev Be-112
Maximum TO Weight (lb)	12500	14000	24259
Payload Weight (lb)	4280	5700	5182
Empty Weight (lb)	6881	8750	
Wing Span (ft)	65	66.67	69.23
Wing area (ft ²)	420	444	547
AR	10.06	10.01	8.76
W/S (lb/ft ²)	29.75	31.53	44.36
TO field Length (ft)	1200		
ROC SL (ft/min)	1600	1350	
Service Ceiling (ft)	25000	24500	
Cruise Speed max (KCAS)	170	187	226
Cruise Speed (KCAS)		157	
Stall speed clean (KCAS)	74		
Stall speed flaps (KCAS)	58		
Range max (nmi)	779		540
Power-to-Weight ratio (hp/lb)	0.12	0.086	0.12

Table 1.2.1. Competitor aircraft parameters

2. Concept selection and Initial sizing

2.1. Aircraft Concept Trade study

Based on mission requirements, the following features of the aircraft must be satisfied:

1. The aircraft must be a top wing aircraft
2. Engines must be mounted such that water spray does not damage the propeller.
3. The cargo door must be big enough to allow cargo to be put into the fuselage and high enough to load cargo in the aircraft being on the water.

Four concepts shown in Figures 2.1.1-2.1.4 were created and scored among each other to determine the best configuration for the current mission.

Concept 1

Concept 1 features a top wing with a conventional empennage configuration. The hull design is also conventional. The cabin and cargo doors are located on the side of the fuselage. One of the cabin doors is a double door used for cargo loading. The engines are located on the wing. Benefits of this design include reliability of the configuration and substantial experience regarding each feature of the aircraft. However, current design lack innovation. In addition, Engines placed on the wings may suffer from excessive water spray, so careful hull design and spray strips addition must be done.

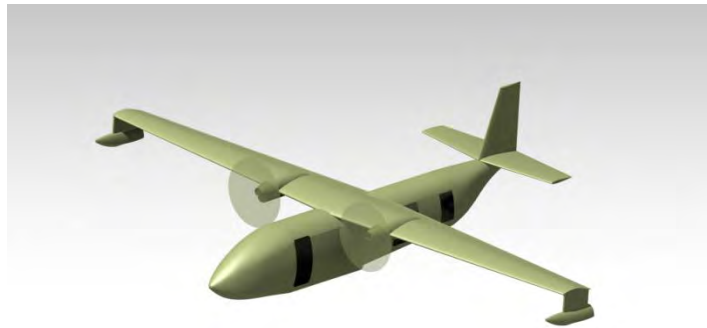


Figure 2.1.1. Concept 1 model

Concept 2

Concept 2 also features a top wing and a conventional hull shape, but it has a twin vertical tail due to a back cargo door which helps load bigger and more irregular cargo shapes. Because of the cargo door, the horizontal tail is put on top of the vertical tail. Engines are put in the vertical tails, so they will not be affected by water spray during take-off and landing. However, trim requirements due to high moment arm produced by the engines and weight penalty due to structural reinforcement of the vertical tail may be significant drawbacks. In addition, the moment arm created by the engine placement

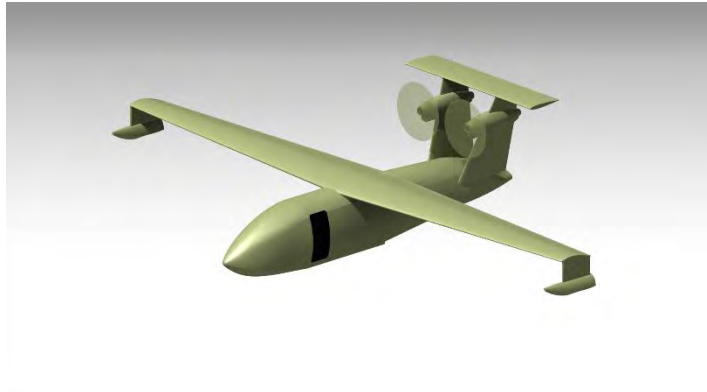


Figure 2.1.2. Concept 2 model

may cause problems during take-off in terms of the aircraft rotation: engines will cause the airplane to pitch down and counteract the elevator to perform the take-off rotation and lift off. Another drawback may include extra effort to deliver fuel to the engine which is placed away from the wings.

Concept 3

Concept 3 features almost same characteristics like Concept 2, but does not have a back cargo door so it features almost all benefits and drawbacks of the Concept 2.

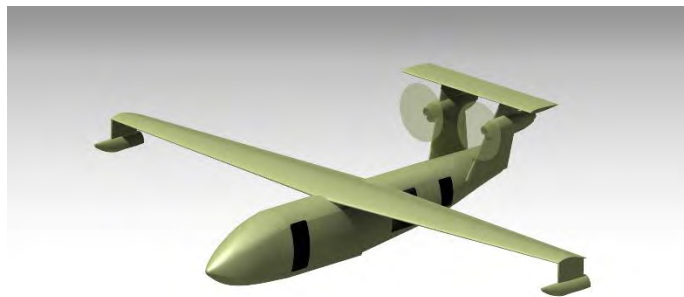


Figure 2.1.3. Concept 3 model

Concept 4

Concept 4 is similar to Concept 1, but it features struts. Although struts may not show a significant difference in the overall configuration comparing to Concept 1, strutted wing may be substantially lighter than the cantilever one, so gross weight of the aircraft may be lower which may affect aircraft performance.

On the other hand, struts may substantially decrease lift-to-drag ratio due to additional drag developed by struts, so performance of the aircraft may be reduced. Careful approximation of the strutted wing parameters such as weight and glide ratio must be considered to determine if this concept shows benefits comparing to others.



Figure 2.1.4. Concept 4 model

To determine the best concept for the current mission, trade study was performed. The concept(s) that satisfy the requirement best get the full score while others get zero. Scores from each requirement are summed and weighted to determine the most suitable aircraft.

Table 2.1.1 presents the trade study results. Concept 1 shows more benefits for the current mission comparing to other aircraft.

	Scale	Concept 1	Concept2	Concept 3	Concept 4
Propeller clearance above the water	1	0	1	1	0
Cargo reload easiness	1	0	1	1	0
Take-off performance	1	1	0		1
Fuel required to complete the mission	1	1	1	1	0
Structural weight penalty	1	1	0	0	0.5
fuel path to engine	0.5	1	0	0	1
Total		3.5	3	3	2

Table 2.1.1. Trade study

However, potential interest was concentrated in concept 4 due to ability to reach a balance between weight and performance that will outperform the conventional concept, so it may outperform Concept 1. To determine whether the Concept 4 has benefits, a series of measurements were done.

After the construction of the Constrained diagram, determination of basic aerodynamics, performance, and flight dynamics, estimation of initial and component breakdown and development of the structural analysis MATLAB code (all details will be discussed in Section 8), it became possible to estimate the effect of struts on the design of the airplane. The key criterion if struts give any benefits to the overall design is the fuel weight ratio. The smaller the ratio is for the same aircraft payload and range, the smaller fuel per passenger will be required which is one of the requirements for the current proposal. Aspect ratio of the wing was fixed and equal to 9. Strut thickness of 25% of the strut chord was assumed and structural analysis was performed on struts at cruise conditions with load factor of three to ensure no failure at given loads. Drag increment due to struts was estimated using Gudmundsson [3]. Results of wing weight, gross weight, drag increment, and fuel-to-weight ratios are shown in Figures 2.1.5 to 2.1.7

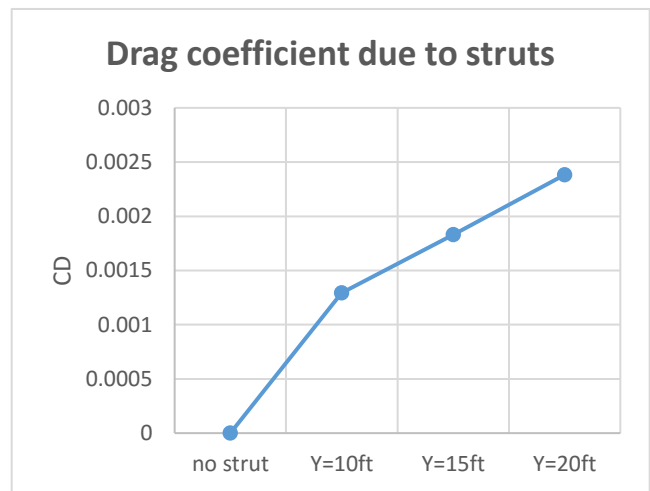
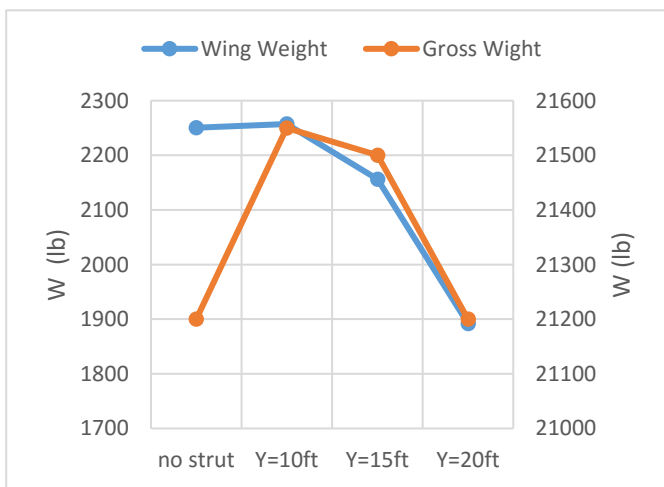


Figure 2.1.5. Weights for different strut configurations

Figure 2.1.6. CD for different strut configurations

Results show that gross weight of the aircraft with struts reaches similar value to the cantilever wing at 20ft spanwise. The wing weight with struts applied reduces with the position of the struts, but the fuel-to-weight

ratio increases with struts due to drag increase, so the struts do not introduce any benefit to the concept and the cantilever wing wins.

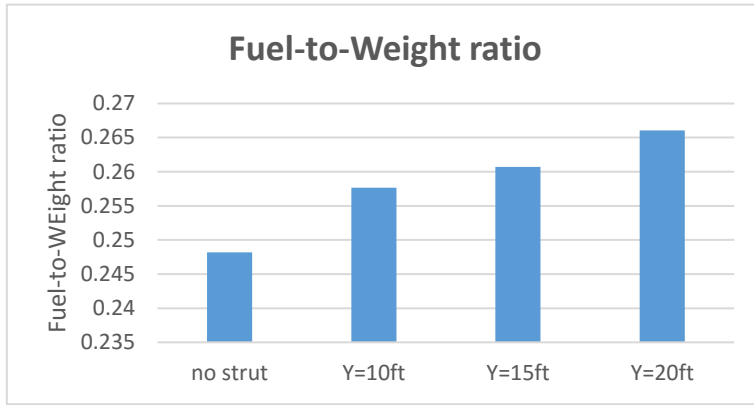


Figure 2.1.7. Fuel-to-Weight ratios for different strut configurations

2.2 Design Sizing and layout

Initial sizing was performed to come up with the initial measurements of the aircraft geometry. Constraint diagram shown in Figure 2.2.1 presents key aircraft performance parameters: cruise, constant-velocity turn, take-off from SL, take-off from 5000ft, climb, and service ceiling. Cruise altitude was chosen to be 16500 ft at SL temperature of +18⁰F. The aircraft performs a 45⁰ constant velocity turn at the

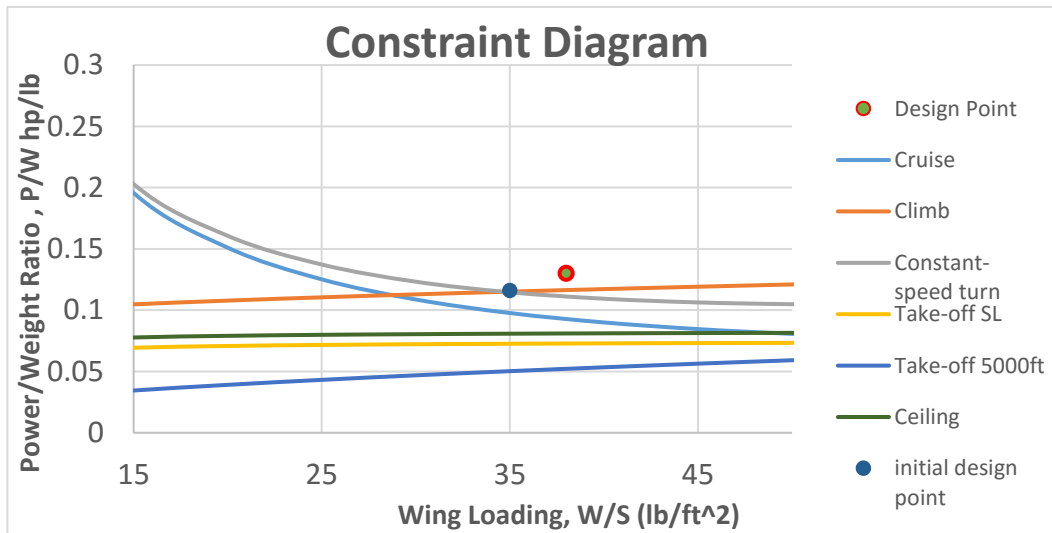


Figure 2.2.1. Constraint diagram

velocity of 215 KTAS. Aspect ratio was initially picked based on the competition experience and was equal to 10, however later it was changed to 9. The efficiency factor of the aircraft was calculated using Raymer [4]. Take-off parameters required for the constraint diagram estimation were picked using both competition study and estimation provided by Gudmundsson[3].

Correction factor based on the operational altitude was approximated to estimate power reduction of the turboprop engine with altitude. All power values were normalized with respect to sea level to adequately represent power required for particular mission maneuvers. Equation below shows the correction formula for the power versus altitude.

$$\frac{P_{alt}}{P_{SL}} = \sigma^n$$

Where σ is a density ratio, and n is a correction coefficient. The correction coefficient was chosen to be 0.7[5] due to lack of information regarding the engine performance at altitude.

Initially, the lowest point on the constraint diagram was chosen to satisfy requirements with minimum power. However, later iterations shifted the initial design point to the position with higher wing and power-to-weight ratio. The final design point specifies power-to-weight ratio of 0.13 and wing loading of 38 psf. Final selection was compared to the competitors to determine credibility of the calculations performed and shows reasonable match.

3. Aerodynamic Design and analysis

3.1. Airfoil Selection

For the wing, a number of NACA NFL airfoils ranging from 12% to 18% thick were considered to come up with a group of best airfoils that would be scored with respect to each other. Experimental results presented in Theory of Wing Section [6] were used to obtain airfoil parameters. Six best airfoils were selected for scoring analysis. All airfoils are 6-series airfoils with different drag bucked range and thickness.

Table 3.1.1 shows airfoil scoring criteria and their characteristics at Reynolds number of nine million. Table 3.1.2 shows scoring results and the winner. The airfoil(s) that perform the best for the particular requirement get one point while others get zero. All scores are added and the airfoil with the greatest amount of points wins. The best airfoil should have the closest lift coefficient at zero AOA to the cruise AOA, should stall gradually at most possible AOA, should have the lowest minimum drag coefficient, closest to zero pitching moment coefficient at cruise, and performance at cruise and climb should be within the drag bucket for more aerodynamic efficiency. Tables 3.1.1 and 3.1.2 show scoring analysis and the final airfoil selection.

Parameters\Airfoil	NACA63(2)-415	NACA63(2)-615	NACA63(3)-418	NACA63(3)-618	NACA65(2)-415	NACA65(3)-418
thickness	15	15	18	18	15	18
Cl0	0.3	0.4	0.3	0.4	0.3	0.3
AOA for Cl=0	-3	-4	-3	-4	-3	-3
Clmax	1.7	1.7	1.6	1.6	1.6	1.5
AOA for Clmax	15	14	16	16	16	18
Stall behavior	A	A	A	A	A	A
Cdmin	0.005	0.005	0.005	0.005	0.004	0.0045
Cl at Cdmin	0.3	0.3	0.3	0.2	0.3	0.2
(Cl/Cd)max	127	150	114	150	140	140
Cl of (Cl/Cd) max	0.7	0.9	0.8	0.9	0.7	0.7
cruise Cm	-0.075	-0.08	-0.08	-0.125	-0.075	-0.075
drag bucket start at Cl	0.2	0.2	0.1	0.2	0.1	0.1
drag bucket end at Cl	0.6	0.8	0.6	0.7	0.7	0.7
CL_ROC in drag bucket	N	Y	N	Y	Y	Y
CL_Cruise in drag bucket	Y	N	Y	N	Y	Y

Table 3.1.1. Airfoil characteristics of best selected airfoils at Re=9 million

Parameters\Airfoil	NACA63(2)-415	NACA63(2)-615	NACA63(3)-418	NACA63(3)-618	NACA65(2)-415	NACA65(3)-418
Cl0	1		1		1	1
AOA for Cl=0	1		1		1	1
Clmax	1	1				
AOA for Clmax						1
Stall behavior	1	1	1	1	1	1
Cdmin					1	
Cl at Cdmin	1	1	1		1	
(Cl/Cd)max		1		1		
Cl of (Cl/Cd) max	1				1	1
cruise Cm	1				1	1
CL_ROC in drag bucket		1		1	1	1
CL_Cruise in drag bucket	1		1		1	1
Sum	8	5	4	3	9	8

Table 3.1.2. Scoring analysis of the airfoils

NACA 65(2)-415 was picked due to the highest score comparing to the competitors. Figure 3.1.1 shows the wing airfoil geometry.

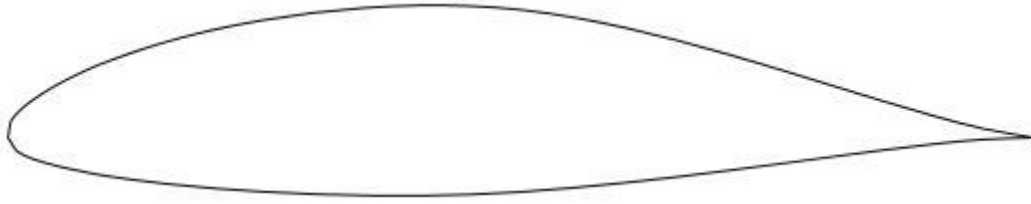


Figure 3.1.1. NACA 65(2)-415 airfoil geometry

Horizontal and vertical tails both feature symmetric airfoils to have symmetric change in lift when an elevator or rudder is used. NACA0012 airfoil was chosen for the horizontal tail, and NACA 0010 was chosen for the vertical tail.

3.2. Wing configuration Design

To approach to elliptic lift distribution and reduce bending moments experienced by the structure, wing and tail taper was applied to the current design. For the wing, taper ratio of 0.5 was decided to be used due to two facts: such taper ratio shows close similarity to the elliptical[4] lift distribution and shift of the highest lift coefficient along the wing span is not too far to reach the aileron, so ailerons are not disabled during stall. Taper ratio of 0.75 and 0.5 were used for horizontal and vertical tails respectively. Figure 3.2.1 and Table 3.2.1 show the layout of the wing and the key parameters.

3.3. Lift analysis

Lift curve slope and maximum lift coefficient of the aircraft were calculated using Raymer[4]. Fuselage effect experienced by the wing was estimated using Torenbeek[7]. To validate theoretical calculations and take fuselage effect on the aircraft more accurately, OpenVSP and VSPAERO Vortex-Lattice package were used to obtain the lift curve. Figure 3.3.1 shows the VSP model of KR-1, Figure 3.3.2 shows the comparison of lift curves obtained from theoretical approach and VSPAERO, Figure 3.3.3 shows lift distribution at

maximum angle of attack, and Table 3.3.1 shows comparison between theoretical estimation of maximum lift coefficient and stall angle of attack and VSP.

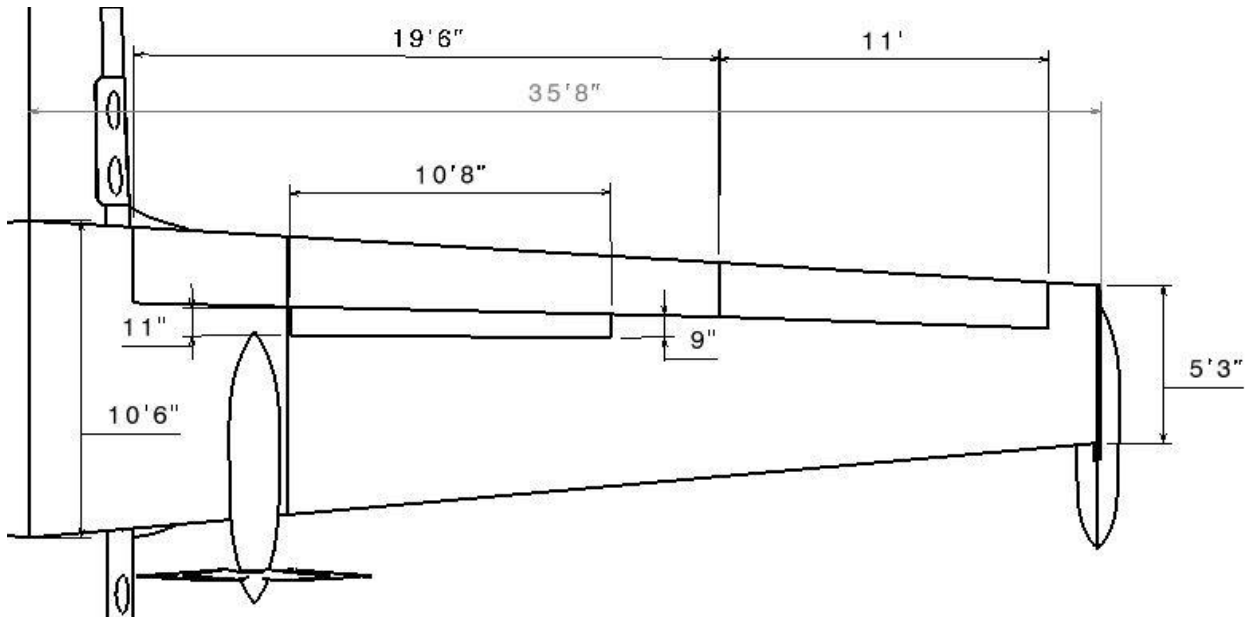


Figure 3.2.1. Wing layout

AR	9
Span	71 ft
Root chord	10.5ft
Taper ratio	0.5
Wing incidence	3°

Table 3.2.1. Wing geometric parameters

Lift coefficient obtained by VSP shows close similarity comparing to theoretical approximation that gives high confidence in lift estimation. Stalling behavior shows that the wing begins to stall in the middle of the wing, but it does not significantly affect the ailerons. Stall angle of attack and maximum lift coefficient for the whole airplane show high similarity between theory and panel methods.

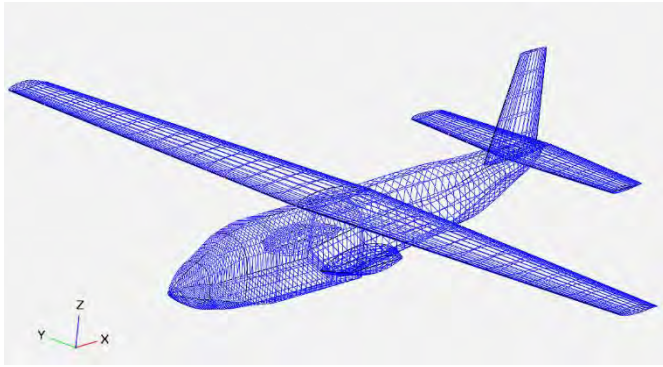


Figure 3.3.1. KR-1 VSP model

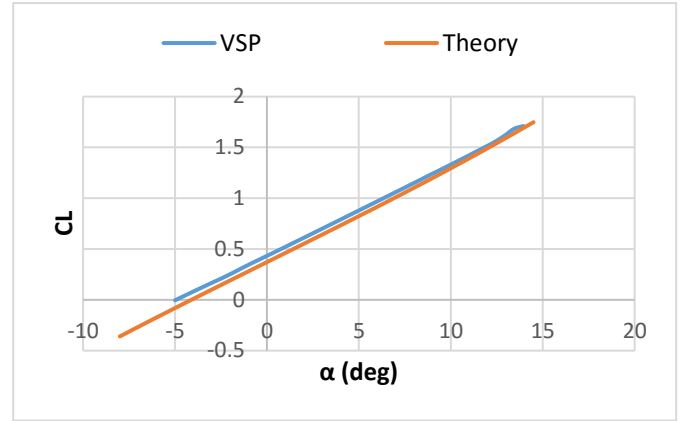


Figure 3.3.2. Lift coefficient comparison

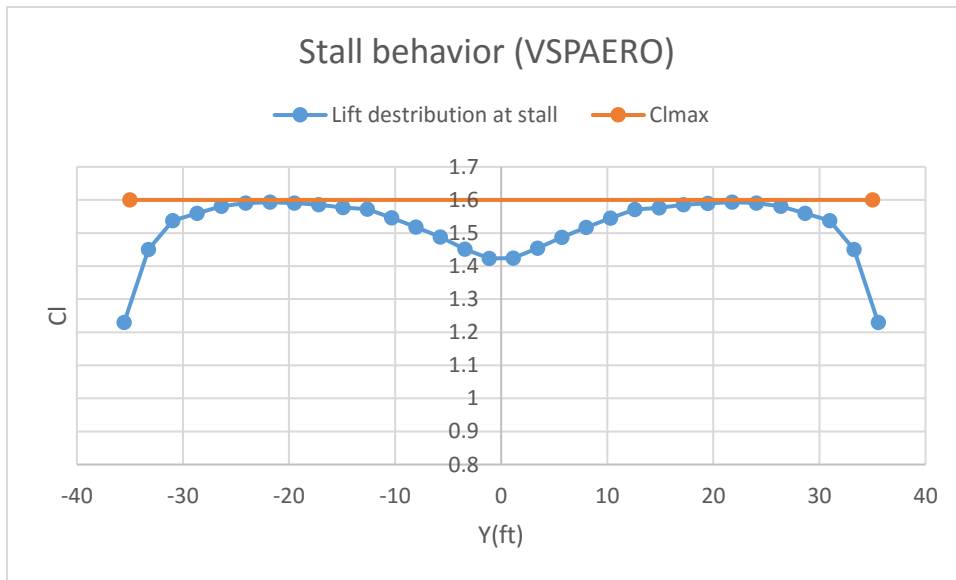


Figure 3.3.3. Lift distribution at maximum AOA from OpenVSP

	Theory	OpenVSP
α_{max}	13.75	13.00
Cl_{max} (whole airplane)	1.67	1.68

Table 3.3.1. Comparison of stall behavior

3.4. Drag analysis

Adjusted drag model shown in Eq (3.4.1) was used to estimate drag produced by the aircraft.

$$C_D = C_{Dmin} + k(C_L - C_{LminD})^2$$

Where C_{Dmin} a combination of pressure is, skin friction and miscellaneous drags and C_{LminD} is lift coefficient at minimum drag.

To consider laminar-turbulent transition while calculating skin-friction drag, Young's method was used. This method considers the position of the boundary layer transition both at the wing root and at the tip and considers roughness. To estimate transition of the laminar boundary layer on the wing and horizontal and vertical tails, CFD calculations were performed for roots and tips. Pointwise grid generation software was used to set up the O-grids for the airfoils. Y^+ value of 1 was used to resolve the boundary layer for each airfoil. Figure 3.4.1 shows an example grid for the wing root chord. ANSYS Fluent solver was used to calculate drag at cruise Reynolds number and zero angle-of-attack. Steady state RANS with Transitional SST turbulence model was utilized to estimate the boundary layer transition. Each solution took around 3500 iterations to reach steady state drag coefficient. Example residuals and pressure are shown in Figure 3.4.2 and Figure 3.4.3 respectively. After the solution was completed, ANSYS post processing tool was used to plot the skin friction coefficient transition for the wing and tails at the top and bottom surfaces at zero AOA. The fuselage was assumed to have a fully turbulent flow. To take into account the shape of the hull and the step, fuselage skin friction drag coefficient was multiplied by a factor of 2. Such estimation gives a conservative value that may be reduced in more deep preliminary design stages. Form factors used for drag calculations were averaged using methods of Raymer, Hoerner, Torenbeek, Shevell, and Jenkinson[1]. In addition, drag contributions due to floats and landing gear fairing was added to the overall parasite drag. Finally, Cumulative result of Undesirable Drag (CRUD) factor of 0.25 was used to take into account additional components that may appear in a final design and affect the drag.

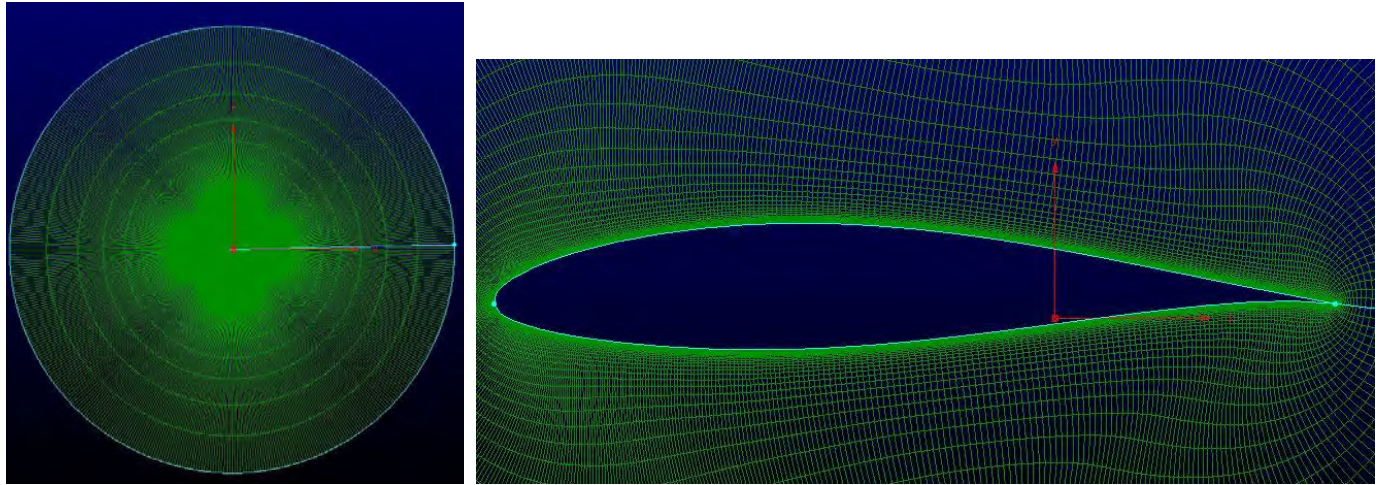


Figure 3.4.1. NACA65(2)-415 O-grid

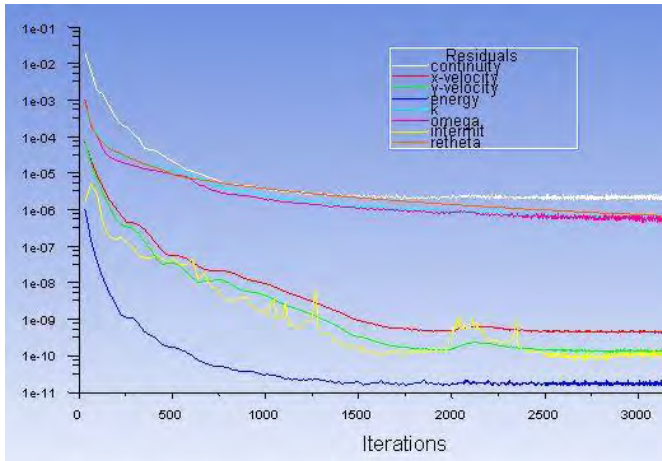


Figure 3.4.2. Solution residuals

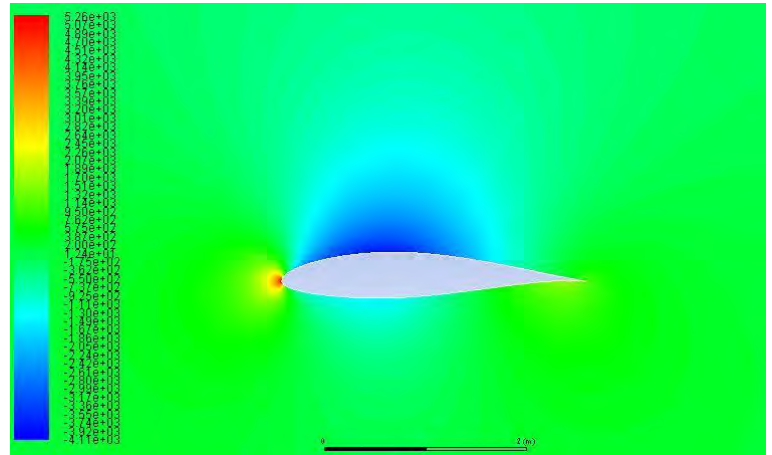


Figure 3.4.3. Airfoil pressure

Wing	
Xcr_Root top/Cr	0.25
Xcr_Root bootom/Cr	0.08
Xcr_Tip top/Ct	0.5
Xcr_Tip Bottom/Ct	0.23

Horizontal tail	
Xcr_Root top/Cr	0.32
Xcr_Root bootom/Cr	0.32
Xcr_Tip top/Ct	0.45
Xcr_Tip Bottom/Ct	0.45

Vertical tail	
Xcr_Root top/Cr	0.3
Xcr_Root bootom/Cr	0.3
Xcr_Tip top/Ct	0.5
Xcr_Tip Bottom/Ct	0.5

Table 3.4.1. Critical boundary layer locations with respect to the chord

Table 3.4.2 and Figure 3.4.1 show drag contribution by each component of the aircraft. Induced drag was calculated taking into account minimum drag lift coefficient. At the preliminary stage, C_{LminD} was obtained

from OpenVSP and was equal to 0.05. Oswald's efficiency was obtained using Raymer and was equal to 0.78.

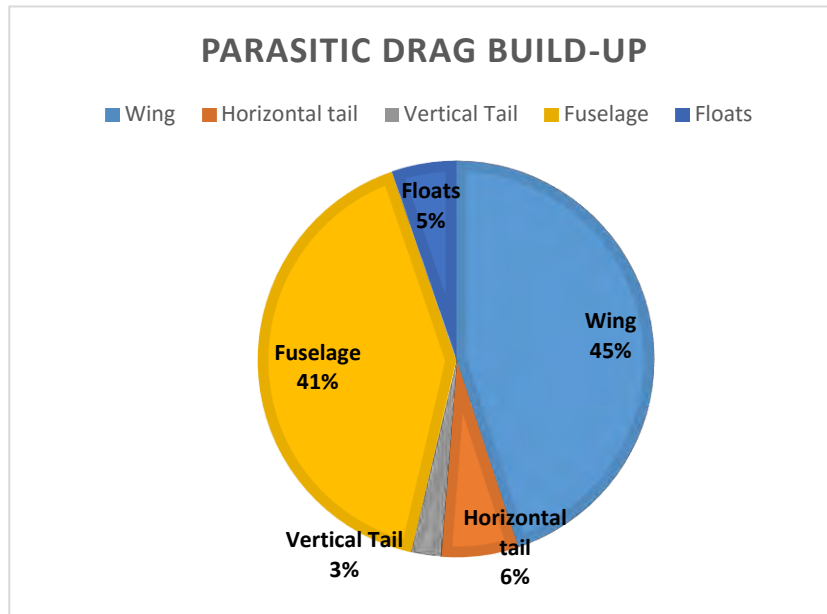


Figure 3.4.1. Parasitic drag build-up at cruise speed

	CDp	Contribution
Wing	0.009	44.95
Horizontal tail	0.001	6.28
Vertical Tail	0.001	2.42
Fuselage	0.009	41.09
Floats	0.001	5.26
CRUD (%)	25.000	

Total	0.026	100
--------------	-------	-----

Table 3.4.2. Parasitic drag build-up at cruise speed

3.5. High-Lift Devices

Due to challenging requirements of the take-off distance both from the ground and the water, extra care must be taken to accurately estimate lift and drag contribution of high-lift devices and correctly determine an appropriate set of devices. After a number of iterations, Fowler flaps were considered as a high-lift device system. Table 3.5.1 shows sizing of the high-lift devices and their lift and drag performances are shown in Figures 3.5.1 and 3.5.2

Flaps		Spoilers	
Flap span ratio	0.55	Spoiler span ratio	0.3
Flap chord ratio	0.30	Spoiler chord ratio	0.10
Flap deflection TO (deg)	20	Spoiler deflection (deg)	45.00
Flap deflection LD (deg)	40		

Table 3.5.1. Geometric layout and of flaps, slats, and spoilers

Torenbeck [7] semi-empirical relations were used to calculate changes in lift and drag due to high-lift devices and Sadraey [8] estimation was used for spoiler performance estimation.

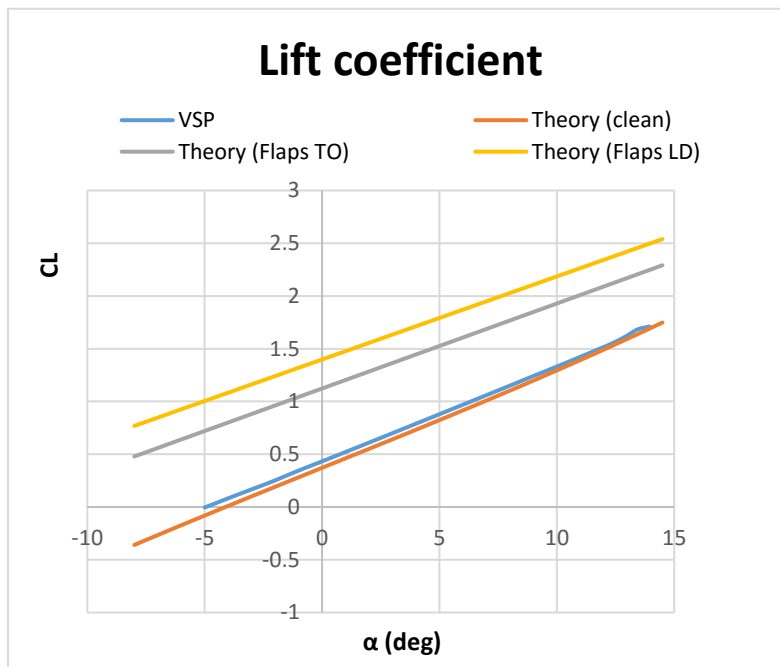


Figure 3.5.1. Lift coefficient for different configurations

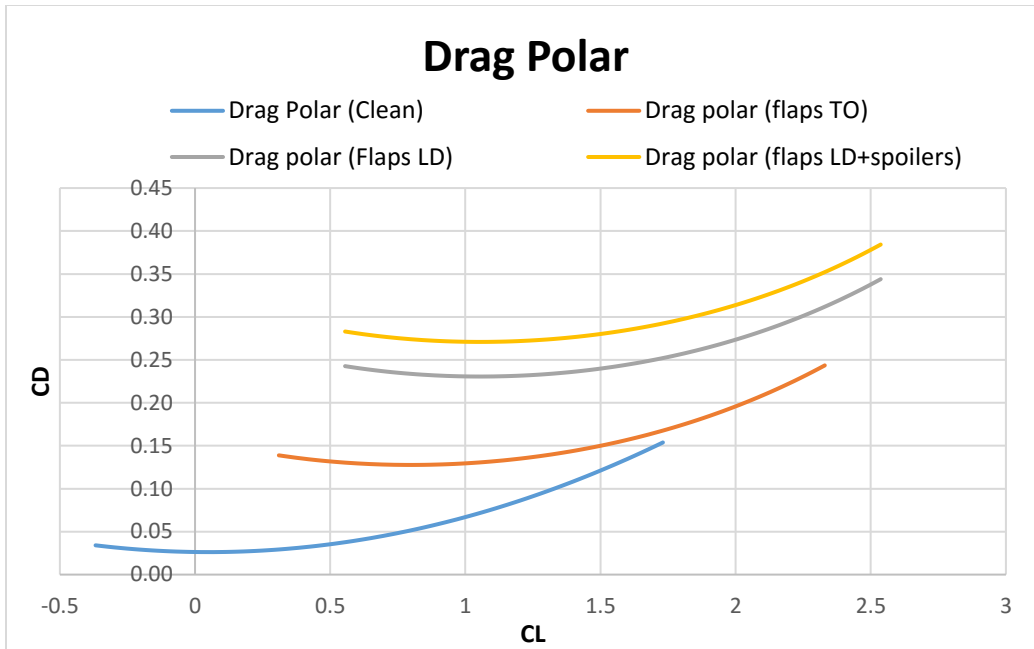


Figure 3.5.2. Drag coefficient for different configurations

Results show increase in lift for both take-off and landing flap configurations with landing flaps producing more lift. Drag polars also look physical showing shift both up and to the left. Finally, maximum lift coefficients for three main configurations (clean, take-off, and landing) were obtained and are shown in Table 3.5.2.

Flight configuration	CLmax
Clean	1.44
Take-off	2.42
Landing	2.68

Table 3.5.2. CLmax for various configurations

3.6. Aerodynamic performance

Aerodynamic performance of the airplane can be represented by lift-to-drag ratio diagram. Figure 3.6.1 shows values of L/D for different configurations. For the clean configuration, lift-to-drag ratio of 10 is

reached at zero AOA and maximum value reaches 15.5. Lift-to-drag ratios for other configurations show substantial drop that is physically real

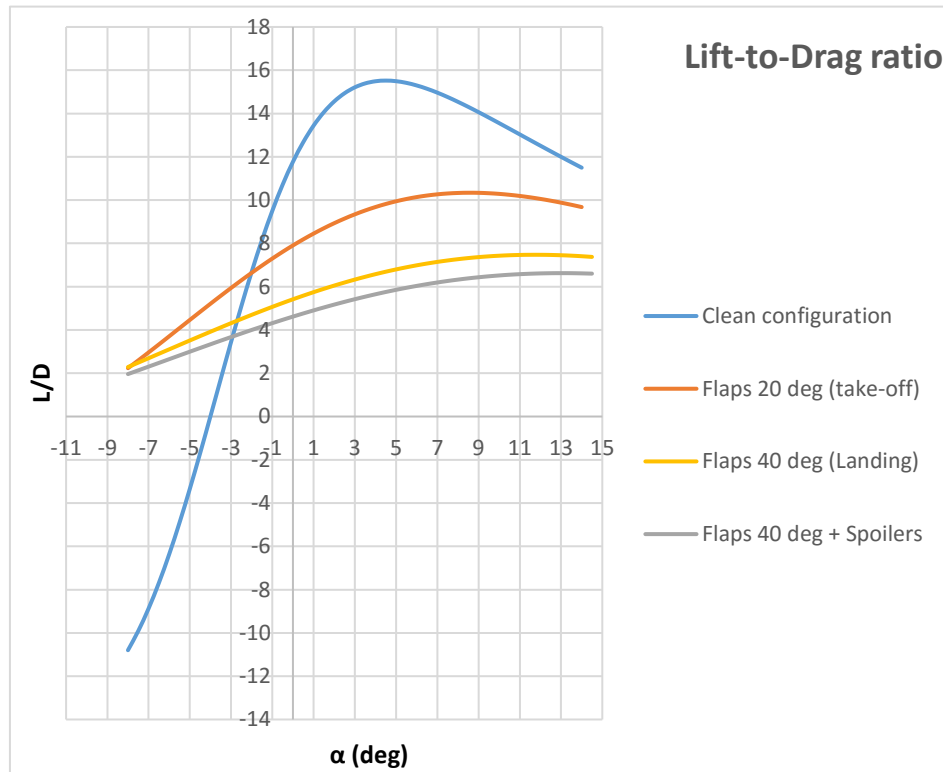


Figure 3.6.1 Lift-to-drag ratio for different aircraft configurations

4. Propulsion

4.1. Engine selection

As long as no constraints were presented by the requirements except availability of the engine, the designer had freedom of selecting any engine type depending on the aircraft performance requirements. Due to significant power requirements, based on the constraint diagram, relatively low Mach number ($M=0.36$), and low operational altitude ($H=16500\text{ft}$), turboprop engines shows the best combination of fuel consumption, power-to-weight ratio and weight comparing to both piston and jet engines. Pratt & Whitney Canada PT6A-68C was chosen as one of the most powerful engine of the most famous family of the

turboprop engines, featuring flat-rated power of 1600SHP, fuel consumption of 0.542lb/h/ehp, and shaft rotation at maximum RPM of 1700. Table 4.1.1 shows PT6A-68C parameters.



Figure 4.1.1. Pratt & Whitney Canada PT6A

Maximum diameter (in)	71.3
Dry Weight (lb)	572
Performance rating (S/L, static) (shp)	1600
Specific Fuel Consumption (lb/h/ehp)	0.542

Table 4.4.1. Pratt & Whitney Canada PT6A-PT6A-68C data

4.2. Propeller analysis and thrust estimation

To get the most benefits from the engine at all stages of the mission, a constant-speed metal propeller with reverse-thrust capabilities was chosen.

Propeller diameter plays an important role in the ability of the engine to transform power produced by the engine into thrust. Two key aspect must be taken into account while choosing the appropriate diameter of the propeller. First, high tip speed must be avoided to prevent losses created by the shocks appearing at the tips. For a metal propeller, maximum Mach number must range between 0.7 and 0.8. Second, spinner may significantly reduce performance of the propeller comparing to an assumption of no spinner effect.

After a number of iterations, propeller diameter was chosen to be 8.25ft. Such diameter gives appropriate amount of thrust for all stages of the mission that satisfies stability requirements and CG range, and prevents the tips from getting shock waves except for the ceiling flight at maximum level speed which is a compromise for better cruise performance. Maximum Mach number was calculated based on maximum RPM of the engine shaft and maximum level speed at a particular altitude discussed in section 7.3. Table

4.2.1 shows Mach numbers at the tip for key mission altitudes. Spinner diameter was assumed one quarter of the propeller diameter based on spinner measurements of other aircraft featuring propeller engine.

	Max tip M
Cruise	0.78
Sea-level	0.73
Ceiling	0.90

Table 4.2.1. Maximum tip Mach number for main flight altitudes

Due to absence of propeller data, thrust analysis on the propeller was performed using momentum theory for cruise conditions and cubic spline for low-speed operations to determine engine performance at take-off and landing. Efficiency and power curves shown in Figures 4.2.1 and 4.2.2 respectively were obtained for the sea-level, 5000ft altitude, cruise altitude, and the ceiling. Maximum efficiency of the propeller was assumed 0.85. In further design iterations, propeller data or the blade-element theory must be used to approximate thrust better.

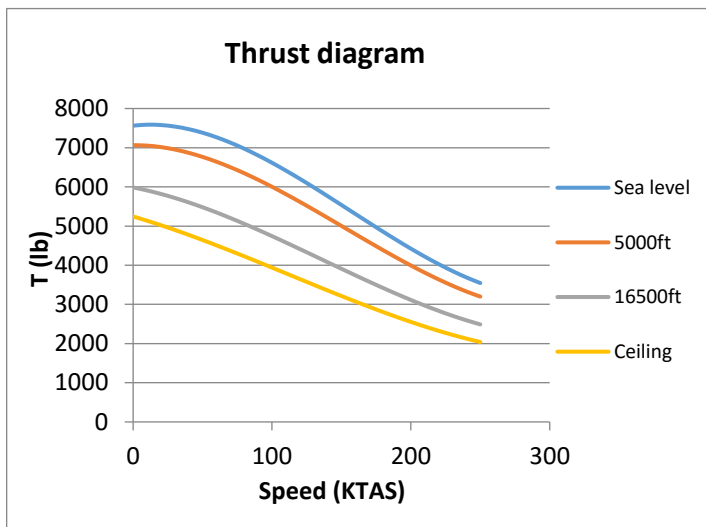


Figure 4.2.1. Thrust output at different altitudes

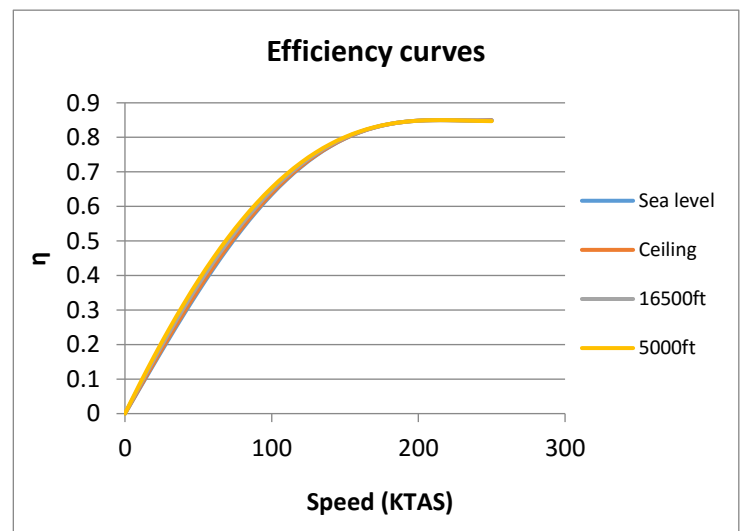


Figure 4.2.2. Efficiency at different altitudes

4.3. Engine Placement

Placement of the engine was determined based on a number of considerations. First, the position of the engine should be limited by the FAR Part 25 requirements: at least one inch between the blade tip and the aircraft structure and 18 inches between the tip and the water must be maintained. Second, danger zones of the propeller determine the position of it with respect to the cabin doors. In addition, water spray and clearance above the water line as well as the static stability must be taken into account while positioning the engine. Finally, and engine-out speed requirements determined by FAR Part 25 and vertical tail sizing play an important role in positioning the engine. Engine placement 7.5 ft away from the aircraft centerline and 1ft above the wing chord line determined after a number of iterations. Figure 4.3.1. shows the engine layout and propeller diameter.

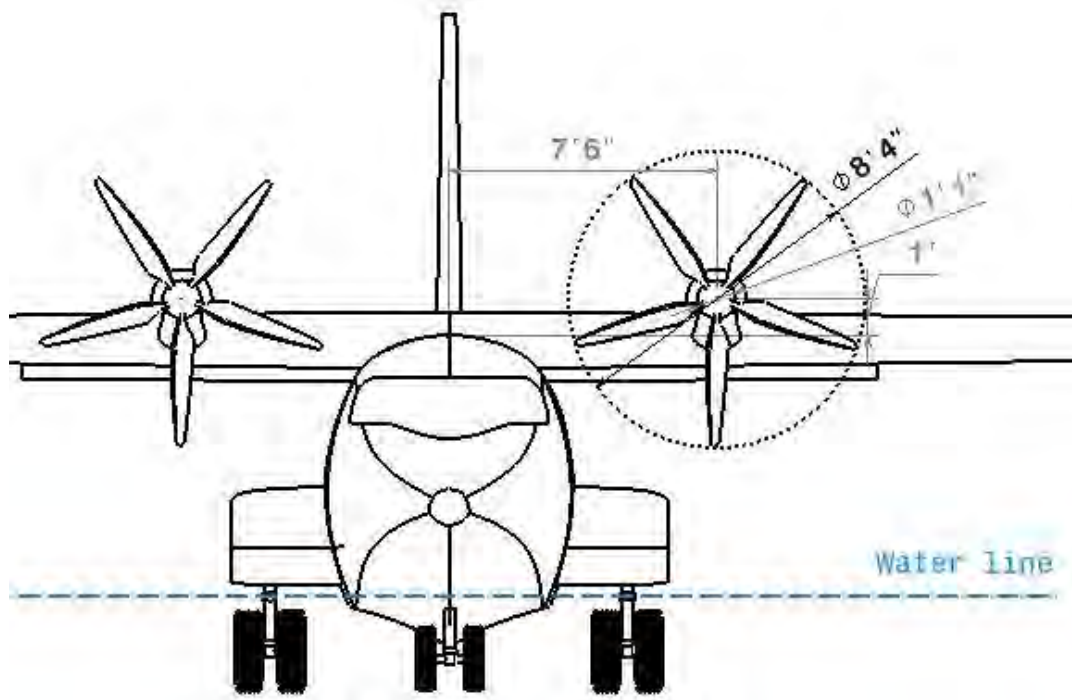


Figure 4.3.1. Engine layout and propeller dimensions.

5. Weights

5.1. Weight Estimations

Gross, empty, and fuel weights of the aircraft were initially determined using take-off weight sizing from Raymer. Fuel-to-weight fractions were calculated from statistical data from Breguet range formula for the longest IFR mission with full passenger capacity presented in Section 2. Empty weight fraction was first estimated using statistical estimations for twin turboprops from Raymer [4]. Maximum take-off weight and Gross weight were assumed to be same, and Maximum landing weight was estimated considering loss of the fuel after take-off. In further stages of design, component weight breakdown of empty weight was used. To estimate weights of each aircraft component more accurately, different methods were considered: Raymer [4], Nicolai [9], and Torenbeek [7]. Average values were obtained to estimate weight of aircraft components. Finally, preliminary weights of the wing and empennage were obtained using stress analysis to increase accuracy of the estimation. For the wing and the empennage, weights obtained from structural analysis were used. Details regarding structural analysis are discussed in Section 8. Tables 5.1.1 and 5.1.2 show weight breakdown for the given design. Weights obtained from structural analysis show close similarity comparing to statistical values.

	Weight (lb)
Maximum take-off Weight	22250
Maximum Landing Weight	21582
Empty Weight	11384
Fuel Weight	5645
Payload Weight	4620
Crew Weight	581

Table 5.1.1. General weight data

Component	Weight %	Weight (lb)
Wing	20.14799	2293.72
Horizontal Tail	2.181941	248.4
Vertical Tail	1.185837	135
Fuselage	28.7974	3278.4
Landing Gear	4.72139	537.5
Engines+Nacelle	15.76953	1795.26
Fuel system	0.939886	107
Flight control system	3.185071	362.6
Avionics	9.506024	1082.2
Anti-icing+AC	2.27795	259.33
Hydraulics	0.195444	22.25
Furnishing	6.967454	793.2
Electrical	4.124079	469.5
Total	1	11384.36

Table 5.1.2. Empty-weight breakdown

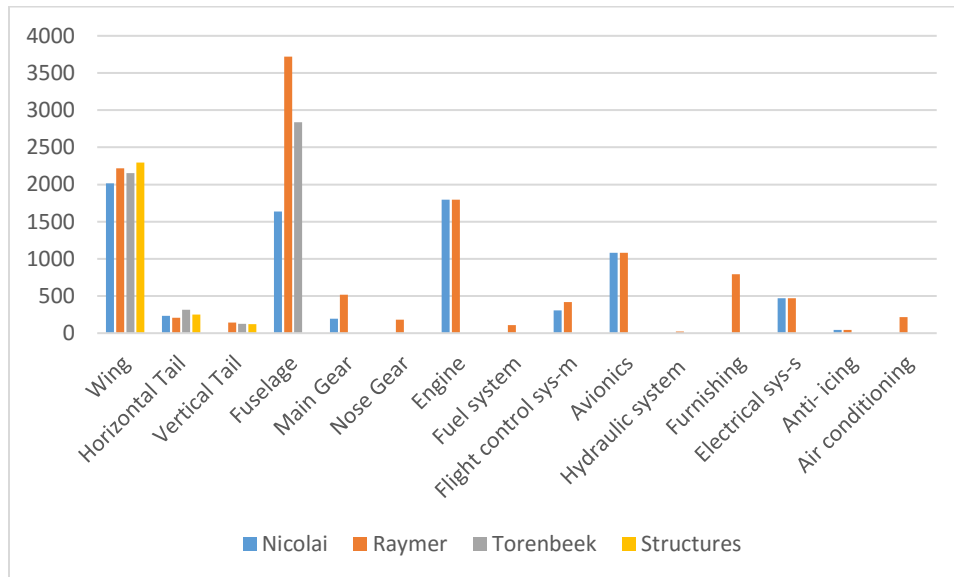


Figure 5.1.1. Weight breakdown comparison using different methods

5.2. Center of Gravity

CG range was calculated for a number of different weight cases. To calculate maximum possible forward and aft CG locations, method provided by Sadraey [8] was used. A MATLAB script reads locations of all components with respect to the aircraft nose and eliminates all removable weights before the CG for the most aft position and after CG for the most forward position. Table 5.2.1 shows CG positions in percent MAC obtained with the MATLAB script. Forward CG limit was determined to be too forward, so trim during take-off and landing is impossible, so the most forward CG case was considered an empty weight. Table 5.2.1 shows an updated CG range, and CG envelope for take-off, landing and cruise conditions is shown in Figure 5.2.1.

	Most fwd cg(ft)	Most aft cg(ft)
Sadraey	20.41	23.63
KR-1	22.18	23.63

Table 5.2.1. CG comparison between Sadraey and KR-1

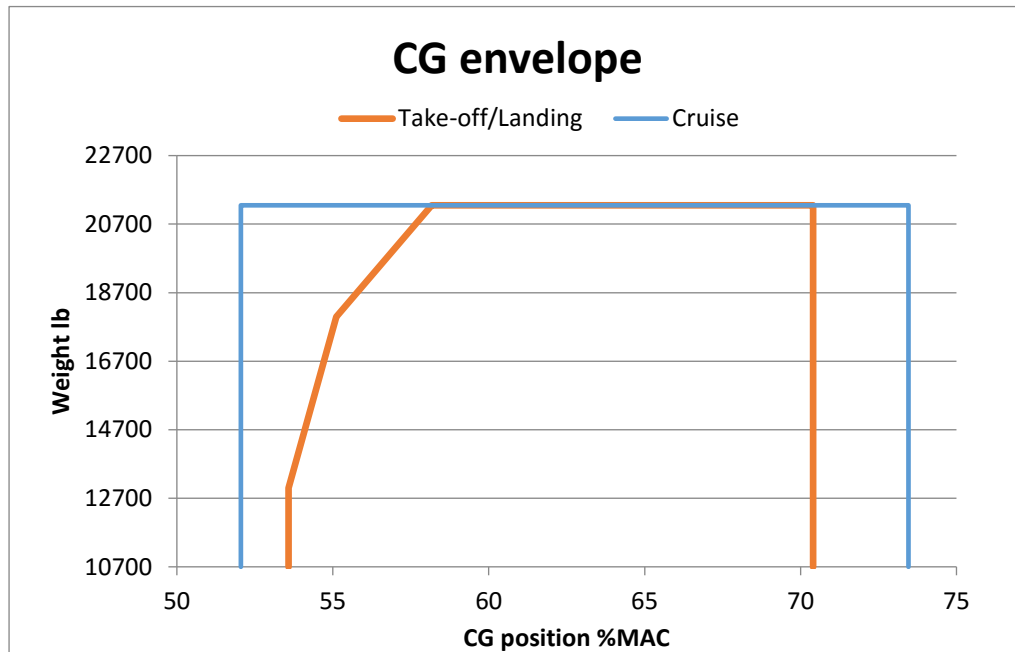


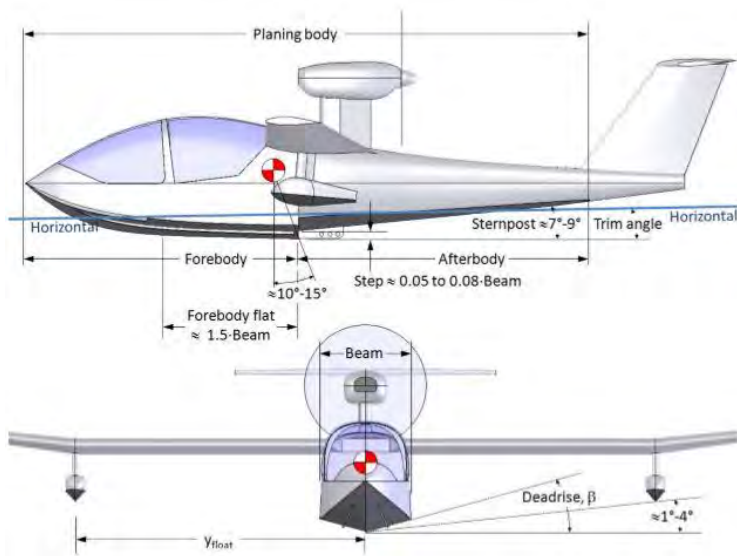
Figure 5.2.1. Load and balance diagram for Take-off, Landing, and Cruise

6. Hull and floats design

6.1. Hull shape Design

Design of a hull plays an important role in many aspects of the aircraft performance. Hull must be designed such that it provides adequate buoyancy for the airplane in the water. FAR Part 25 [10] requires the hull to be able to withstand 1.8 gross weights of the airplane. In addition, performance of the airplane during take-off and landing highly depends on the hull geometry: lengths of the forebody and aftbody; location, type, and height of the step required for the airplane transition during take-off; deadrise angle; existence of flare etc. Details and decision making regarding design of each component of the hull will be described in below.

Figure 6.1.1 shows nomenclature of a common hull and Figures 6.1.2 and 6.1.3 show layout and dimensions of the KR-1 hull. Volume of the hull depends on the gross weight of the aircraft including FAR Part 25 requirements, and geometric constraints of the airplane such as the airplane length and width. Longer and



narrower hulls (beam-to-length ratio of 10 and above) show superior performance during take-off due to their lower resistance. However, such hull shapes become problematic for transport airplanes that require particular internal layout and CG range requirements. Given aircraft features common length-to-beam ratios ratio of 5.76 that provides appropriate internal dimension

Figure 6.1.1. Hull nomenclature and common dimensions [3]

of the aircraft for the mission. Hull volume was obtained with the idea to be able to load the airplane on both the water and land which is crucial for water airports. Water clearance should be big enough to open the cabin doors and load cargo or passengers. To calculate the clearance, water draft must be obtained.

Draft was calculated applying Archimedes principle and geometric properties of the aircraft (Gudmunsson) and was 1.59ft.

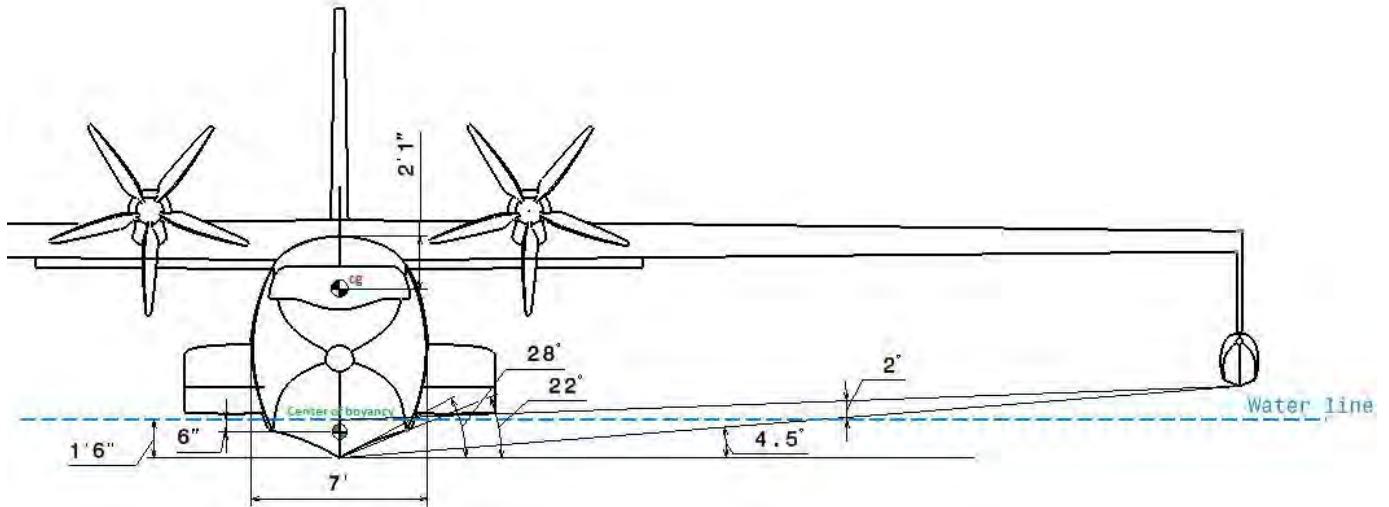


Figure 6.1.2. Front view and hull dimensions

Center of buoyancy was initially calculated theoretically and was more accurately determined with CATIA at later stages of the design.

Hull bottom design shape depends on several factors: take-off requirements, stability and control, load factors, water spray, and draft. More flat hull bottoms show superior performance during take-off and smaller draft values comparing to sharper shapes. However, bottoms that are more flat behave less stable in wavy weather conditions and experience higher loads during landing which causes structural reinforcement and weight increase. In addition, bottoms that are more flat generate more spray that may reach the engine and cause severe problems.

FAR Part 25 specifies reaction load factors required to be tolerated by a hull with particular characteristics

$$n_w = \frac{C_1 V_{s0}^2}{(\tan^{2/3} \beta) W^{1/3}}$$

Where n_w is a water reaction load factor, C_1 is a seaplane operations factor equal to 0.012, V_{s0} is stall

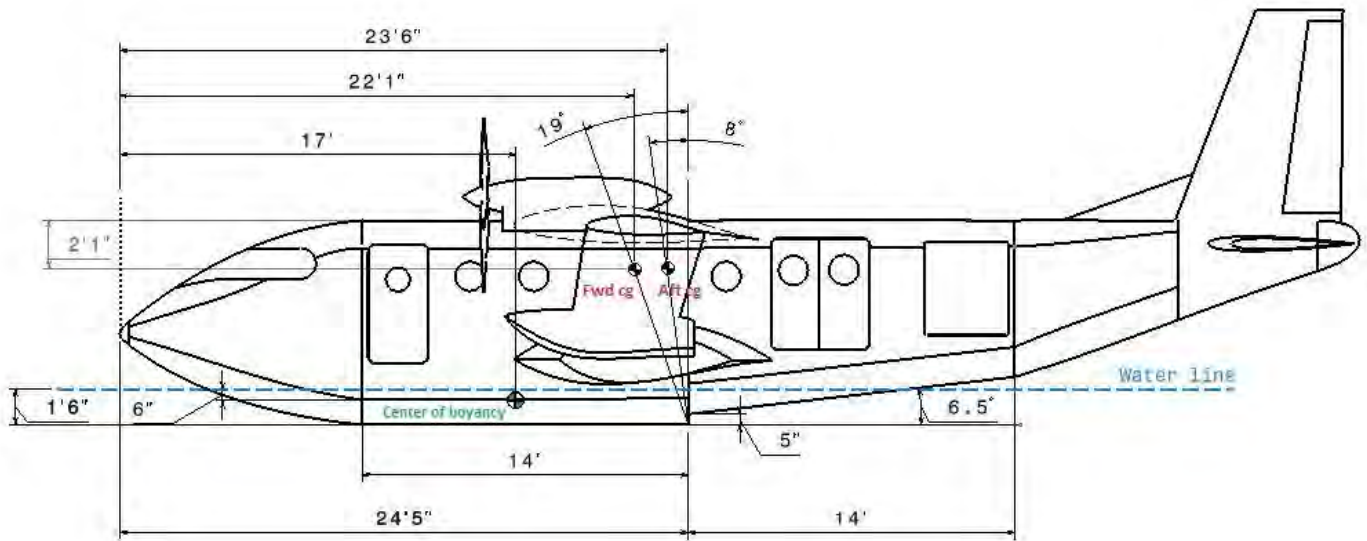


Figure 6.1.3 Side view and hull dimensions

speed with high-lift devices deflected, β is deadrise angle, and W is maximum aircraft landing weight. Figure 6.1.4 shows a plot of load factors with respect to stall speeds depending on deadrise angle and the design point. After a number of iterations, load factor of 3.1 was obtained as an appropriate value depending on the deadrise angle of 22° to mitigate draft and stall speed discussed below.

Forebody and aftbody lengths, sternpost angle, and step geometry depend on spray requirements and stability of the airplane during take-off. Empirical relations shown in Figures 6.1.5-6.1.8 [11] show relations between key parameters of the hull. From figure 6.1.5, buoyancy force coefficient is defined by

$$C_W = \frac{W}{\rho_w B^3}$$

Where ρ_w is water density and B is the hull beam.

Coefficient K is defined by

$$K = \frac{W}{\rho_w B L_f^2}$$

Where L_f is forebody length.

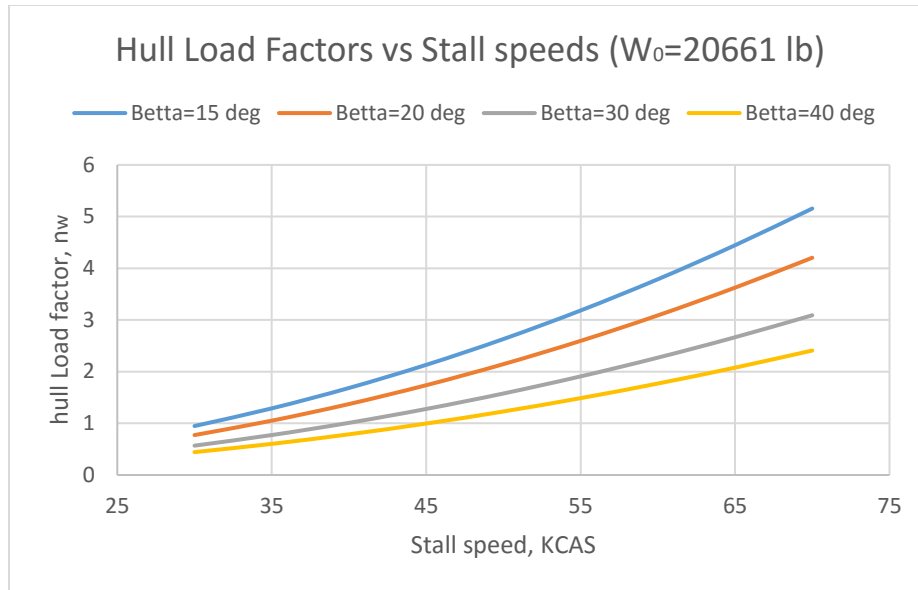


Figure 6.1.4. Hull load factor vs stall speeds at different deadrise angles for landing configuration

Considering geometric constraints, it was concluded that the current design cannot reach values of K corresponding to acceptable spray, so possible design solutions include introduction of flare of the hull bottom to turn the spray away from the engine. In addition, spray strips should be considered for more detailed design as a device mitigating spray height. Step was put such that angle between CG's and the step is within 10-15 degrees as specified in Gudmundsson [3]. Forebody flat length was chosen to be equal to two beam.

Mission also requires the airplane to be able to withstand sea state 3 conditions. Maximum wave height can be estimated by

$$h_{wave} = 1.25 \ln(W) - 8.6414$$

Table 6.1.1 shows requirements for sea state 3 and maximum wave height. Maximum wave height falls into seastate 3 and covers almost all the region of state 3. However, further analysis must be obtained to determine actual value of maximum wave height

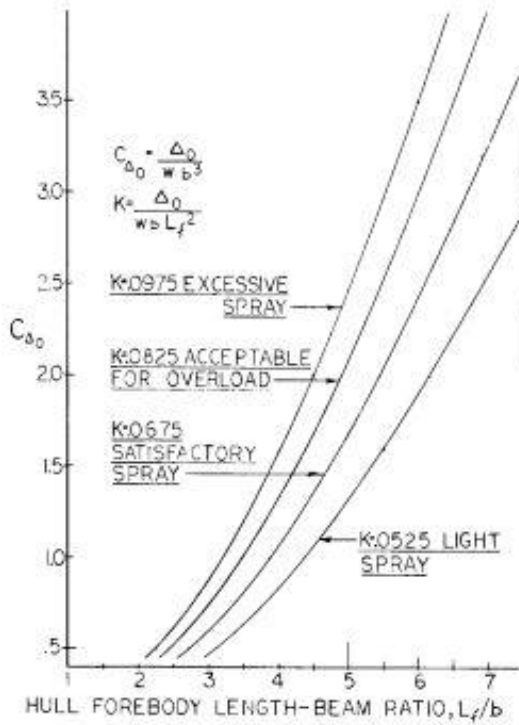


Figure 6.1.5. Weight coefficient relation

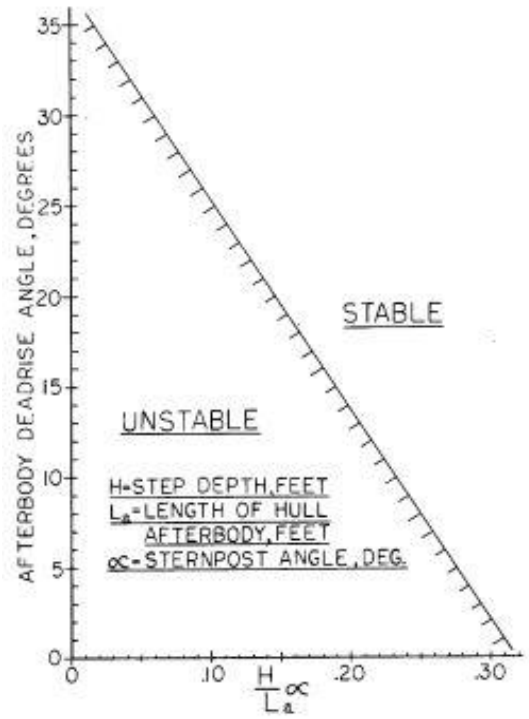


Figure 6.1.6. Afterbody deadrise angle relation

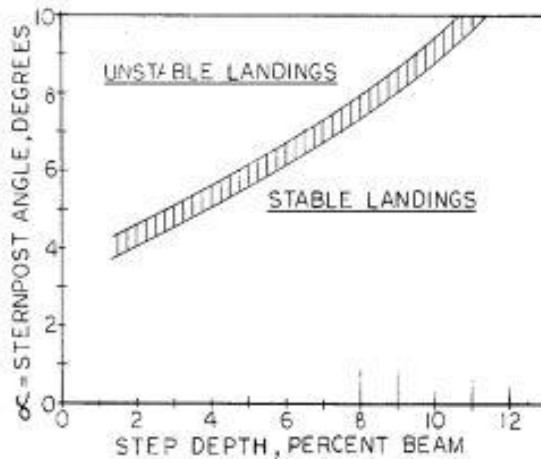


Figure 6.1.7. Sternpost angle vs step depths

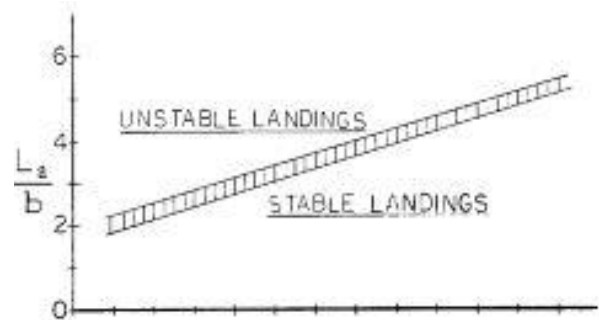


Figure 6.1.8. Afterbody-to-beam ratio vs step depth

	Wave height (ft)
Sea State 3 Minimum	1.67
Sea State 3 Maximum	4.08
Maximum of KR-1	3.87

Table 6.1.1. Sea State 3 requirements and maximum wave height for KR-1

6.2. Floats design

To ensure lateral stability of the aircraft on the water, a top-wing aircraft frequently requires floats. The geometric design of the float follows the same FAR Part 25 requirements and approach as the hull, although the step is not needed for the floats. The key parameters of the floats are the volume of the float, the deadrise angle, and the location of the floats with respect to the span. To calculate the displacement weight of the float, the following expression [12] is used

$$1.8W_h \sin\theta = W_f l_f \cos\theta$$

Where W_f and l_f are the displacement weight of the float and float position along the span respectively and θ is the lateral inclination angle before the float is submerged. Based on the formula, a set of solutions for

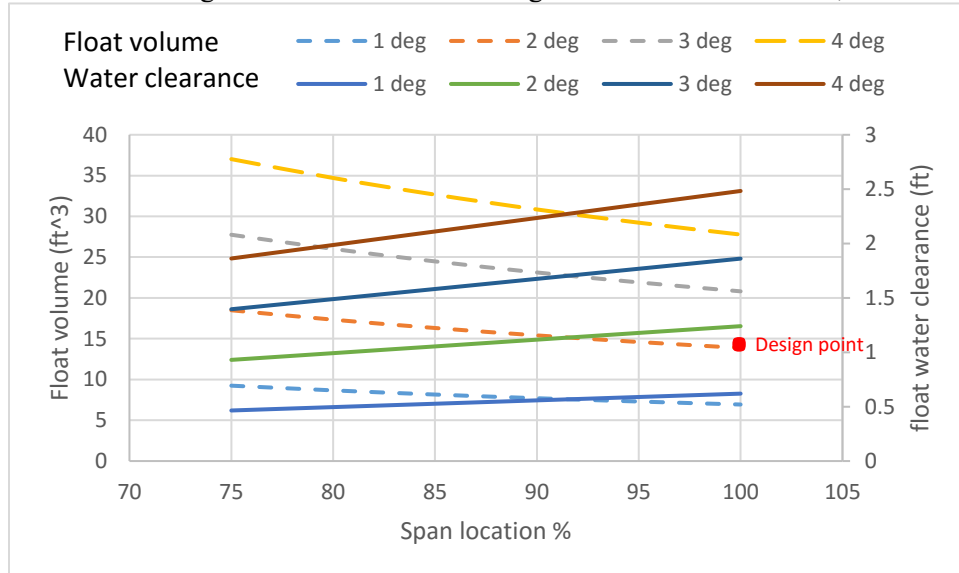


Figure 6.2.1. Float volume and water clearance vs float location

the displacement weight and then for the float volume can be found. Smaller float volume generates less drag, so a smaller float is preferable. Figure 6.2.1 shows float volume appropriate for floats at particular each locations along the wing span and inclination angles. In addition, the figure presents water clearance for float combination.

Based on examples of aircraft such as Beriev Be-200, Grumman Mallard, and Beriev Be-112, approximately, 1 ft of water clearance works well, so inclination of 2° was chosen for KR-1. As for the span location, the float was decided to be put at the wingtip to work as a wingtip device to reduce the induced drag giving the float volume of 13.86 ft^3 , although the float volume becomes greater at the same inclination angle and structural reinforcement may be used. An optimization study with must be performed to determine the best location of the float to achieve a compromise. The deadrise angle of 23° was chosen based on approach used for the hull design. The float diagram is shown in Figure 6.2.2.

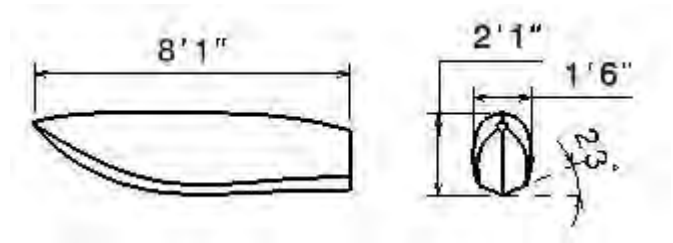


Figure 6.2.2. Float layout and dimensions

7. Aircraft performance

Performance analysis consists of a number of cases required for the current proposal. First case demonstrates 250 nmi STOL runway mission with 20 passengers with take-off and landing from the ground at sea level and 5000ft at ISA +18°F and for different runway profiles. Second case demonstrates a 250 nmi STOL water mission with 20 passengers with take-off and landing from the water at sea level and 5000ft at ISA +18°F. Third case presents a 1000nmi mission with maximum amount of passengers with ground and water take-off and landing at sea level at ISA +18°F. Final case shows a 500nmi cargo mission with ground and water take-off and landing at sea level at ISA +18°F. In addition, a payload range-relationship will be discussed.

7.1. Take-off and Landing

Take-off and landing requirements became ones of the most critical variables that determined the aircraft layout. Short take-off and landing requires the lowest possible aircraft weight, strong aerodynamic characteristics of the aircraft as well as a powerful propulsion system. To perform take-off and landing

analysis, key aircraft airspeeds must be determined. Table 7.1.1 shows different speed obtained for the current aircraft following FAR Part 25 requirements.

Take-off			Landing		
	Requirement	Speed (KCAS)		Requirement	Speed (KCAS)
V_{SR}	$V_{SR} \geq V_{CLmax}$	67.25	V_{SR}	$V_{SR} \geq V_{CLmax}$	62.75
V_{MC}	$V_{MC} \geq 1.13 V_{SR}$	70.5	V_{FLR}	$V_{FLR} < 1.23 V_{SR}$	75.3
V_R	$V_{MR} \geq 1.05 V_{SR}$	72	V_{TD}	$V_{TD} < 1.1 V_{SR}$	69
V_{LOF}	$V_{LOF} \approx 1.1 V_{SR}$	74	V_{BR}	$V_{BR} < 1.1 V_{SR}$	69
V_{2min}	$V_{2min} \geq 1.13 V_{SR}$	76			

Table 7.1.1. FAR Part 25 speed requirements and values

7.1.1. Ground take-off and landing

Ground take-off was estimated using dynamic and kinematic equations from classical mechanics. After the aircraft reached rotation speed, transition length was estimated to be $1.5 V_{LOF}$ [3]. 50ft obstacle performance was calculated using Gudmundsson's approach [1]. Figure 7.1.1 shows ground run example for the 250nmi STOL mission with 20 passenger at sea level, and Tables 7.1.2 and 7.1.3 show lengths of each section of take-off and total take-off distance profiles for all performance cases from sea level and 5000ft respectively. Results for the STOL case show that the aircraft is capable of taking off within 1500ft with 50ft obstacle, so the requirement is satisfied.

Landing performance was estimated using dynamic and kinematic equation as used for the take-off. Three degrees approach angle was assumed to estimate the approach distance. In addition, reverse thrust equal to 60% of engine's static thrust was assumed [3]. Tables 7.1.4 and 7.1.5 show lengths of each stage of landing as well as total landing distance for each performance case. Results for the STOL cases show that the aircraft is capable of landing within 1500ft with 50ft obstacle, so landing requirement is also satisfied.

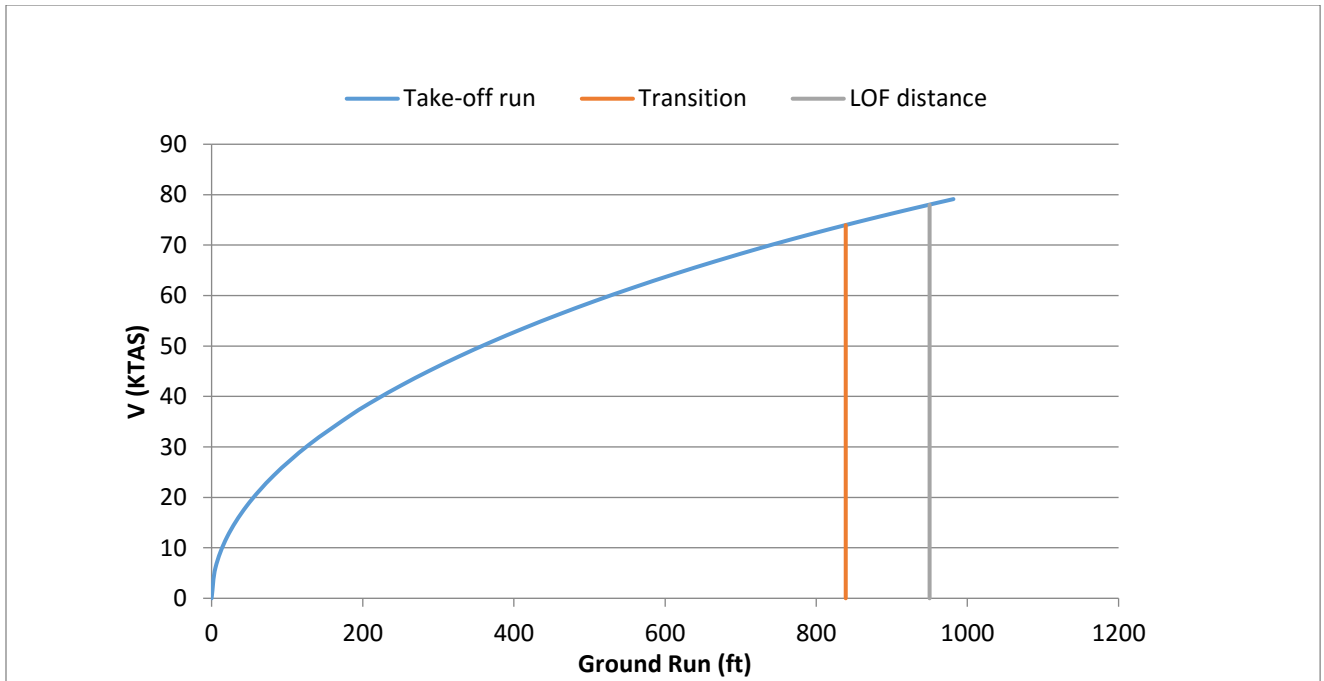


Figure 7.1.1. Take-off run for for the 250nmi STOL mission with 20 passenger at sea level

Sea Level				
250 nmi mission				
Surface properties	Ground run (ft)	Transition (ft)	50 ft obstacle run (ft)	Total (ft)
dry concrete/asphalt	840	111	525	1476
wet concrete/asphalt	857	111	525	1493
wet grass	920	111	525	1556
firm dirt	840	111	525	1476
soft turf	904	111	525	1540
1000 nmi mission				
Surface properties	Ground run (ft)	Transition (ft)	50 ft obstacle run (ft)	Total (ft)
dry pavement	853	111	525	1489
500 nmi mission				
Surface properties	Ground run (ft)	Transition (ft)	50 ft obstacle run (ft)	Total (ft)
dry pavement	846	111	525	1482

Table 7.1.2. Ground take-off distance data for different mission cases at sea level

5000 ft				
250 nmi mission				
Surface properties	Ground run (ft)	Transition (ft)	50 ft obstacle run (ft)	Total (ft)
dry concrete/asphalt	923	111	524.6	1558.6
wet concrete/asphalt	945	111	524.6	1580.6
wet grass	1025	111	524.6	1660.6
firm dirt	923	111	524.6	1558.6
soft turf	1005	111	524.6	1640.6
1000 nmi mission				
Surface properties	Ground run (ft)	Transition (ft)	50 ft obstacle run (ft)	Total (ft)
dry pavement	940	111	525	1576
500 nmi mission				
Surface properties	Ground run (ft)	Transition (ft)	50 ft obstacle run (ft)	Total (ft)
dry pavement	930	111	525	1566

Table 7.1.3. Ground take-off distance data for different mission cases at 5000ft.

Sea level					
250 nmi mission					
Surface properties	Approach distance (ft)	Flare distance (ft)	Free-roll distance (ft)	Braking distance (ft)	Total
dry concrete/asphalt	656	118	104	423	1301
wet concrete/asphalt	656	118	104	560	1438
wet grass	656	118	104	505	1383
firm dirt	656	118	104	471	1349
soft turf	656	118	104	505	1383
hard turf	656	118	104	366	1244
1000 nmi mission					
Surface properties	Approach distance (ft)	Flare distance (ft)	Free-roll distance (ft)	Braking distance (ft)	Total
dry pavement	656	118	104	423	1301
500 nmi mission					
Surface properties	Approach distance (ft)	Flare distance (ft)	Free-roll distance (ft)	Braking distance (ft)	Total
dry pavement	656	118	104	423	1301

Table 7.1.4. Ground landing distance data for different mission cases at sea level

5000 ft					
250 nmi mission					
Surface properties	Approach distance (ft)	Flare distance (ft)	Free-roll distance (ft)	Braking distance (ft)	Total
dry concrete/asphalt	656	118	104	433	1311
wet concrete/asphalt	656	118	104	555	1433
wet grass	656	118	104	507	1385
firm dirt	656	118	104	433	1311
soft turf	656	118	104	507	1385
hard turf	656	118	104	380	1258

1000 nmi mission					
Surface properties	Approach distance (ft)	Flare distance (ft)	Free-roll distance (ft)	Braking distance (ft)	Total
dry pavement	656	118	104	433	1311

500 nmi mission					
Surface properties	Approach distance (ft)	Flare distance (ft)	Free-roll distance (ft)	Braking distance (ft)	Total
dry pavement	656	118	104	433	1311

Table 7.1.5. Ground landing distance data for different mission cases at 5000ft

7.1.2. Water take-off and landing

Water take-off and landing becomes a challenging task when hydrodynamic performance parameters of the hull such as water resistance and hull trim angle at different speed are unknown. To predict take-off and landing distances for the aircraft, trim angle and hull resistance coefficient were estimated using

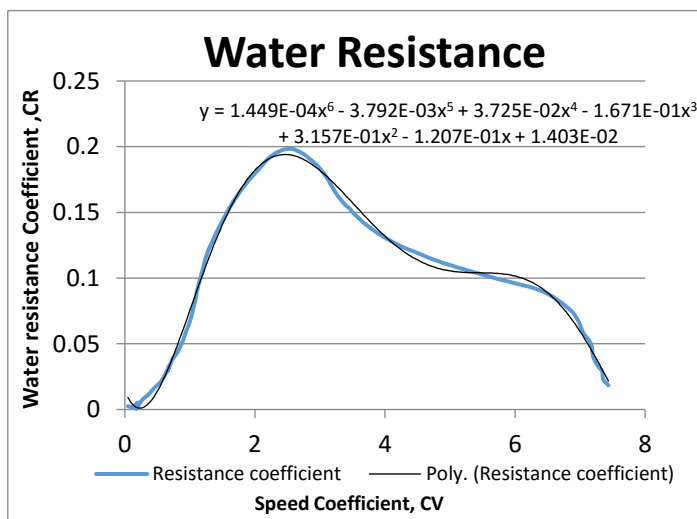


Figure 7.1.2. Water hull resistance estimation

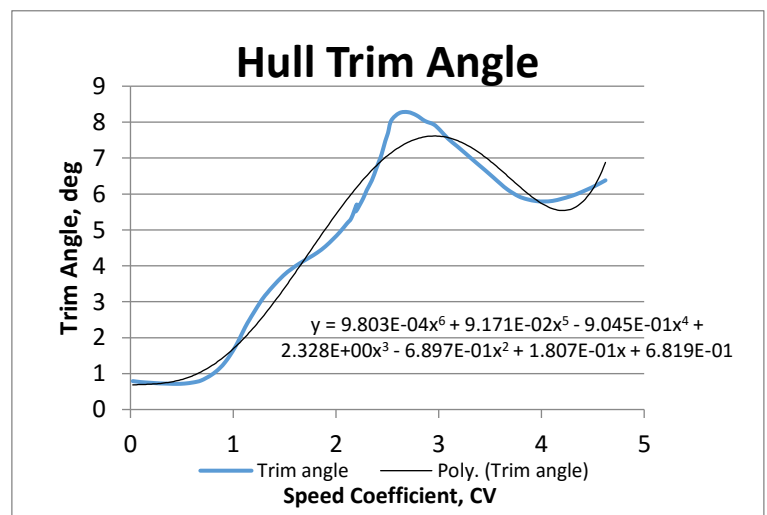


Figure 7.1.3. Trim angle estimation

experimental data from Reference [13] for a conventional hull case. Figures 7.1.2 and 7.1.3 show water resistance coefficient and trim angle

relation for a conventional hull. In addition, a number of assumptions were made:

1. Reduction of resistance with decrease of draft due to lift is estimated by

$$C_{R\Delta} = C_R \frac{C_{\Delta}}{C_{\Delta 0}}$$

Where $C_{\Delta 0}$ the load coefficient at the take-off and rest is, C_R is a resistance coefficient, and C_{Δ} is a load coefficient.

2. Once the speed coefficient exceeds 7.5, water resistance coefficient becomes zero according to Figure 7.1.2. The airplane may not be airborne at this moment, but it is hydroplaning, so Froude frictional resistance must be considered. Froude resistance can be calculated by

$$R_{Froude} = f S_{wet} V^n$$

Where f is a coefficient of frictional resistance conservatively assumed to be 0.015, S_{wet} is wetted area assumed to be four beam lengths, V is speed in knots, and n is a surface quality coefficients assumed to be equal to 2.

3. Pilot slowly increases thrust and reaches full throttle within 10 seconds. Throttle factor is assumed by

$$r = \begin{cases} 0.25 + 0.75 \left(\frac{t}{10} \right), & t < 10s \\ 1, & t \geq 10s \end{cases}$$

Tables 7.1.6 and 7.1.8 shows take-off and landing distances using assumptions made above. STOL missions requirements of maximum take-off and landing distances of 1900ft are satisfied.

Sea Level			5000 ft		
250 nmi mission			250 nmi mission		
Water run distance (ft)	50 ft obstacle run (ft)	Total	Water run distance (ft)	50 ft obstacle run (ft)	Total
921	524.6	1445.6	1050	524.6	1574.6
1000 nmi mission			1000 nmi mission		
Water run distance (ft)	50 ft obstacle run (ft)	Total	Water run distance (ft)	50 ft obstacle run (ft)	Total
1200	524.6	1724.6	1386	524.6	1910.6
500 nmi mission			500 nmi mission		
Water run distance (ft)	50 ft obstacle run (ft)	Total	Water run distance (ft)	50 ft obstacle run (ft)	Total
1046	524.6	1570.6	1243	524.6	1767.6

Table 7.1.6. Water take-off distance data for different mission cases at sea level and 5000ft

Sea Level			
250 nmi mission			
Approach distance (ft)	Flare distance (ft)	Braking distance (ft)	Total
656	118	704	1478
1000 nmi mission			
Approach distance (ft)	Flare distance (ft)	Braking distance (ft)	Total
656	118	770	1544
500 nmi mission			
Approach distance (ft)	Flare distance (ft)	Braking distance (ft)	Total
656	118	745	1519

Table 7.1.7. Water landing distance data for different mission cases at sea level

5000 ft			
250 nmi mission			
Approach distance (ft)	Flare distance (ft)	Braking distance (ft)	Total
656	118	752	1526
1000 nmi mission			
Approach distance (ft)	Flare distance (ft)	Braking distance (ft)	Total
656	118	820	1594
500 nmi mission			
Approach distance (ft)	Flare distance (ft)	Braking distance (ft)	Total
656	118	795	1569

Table 7.1.8 Water landing distance data for different mission cases at 5000ft

7.2 Climb

Climb performance shown in Figure 7.2.1 demonstrates climb performance for the 1000nmi mission weight with full payload. Both sea level and cruise altitude performance capabilities are shown. Maximum rate-of-climb at sea level reaches 3000fpm at 135 KCAS that is a high value comparing to the competitors. Climb performance at cruise altitude shows maximum value of 1841 at 115 KCAS.

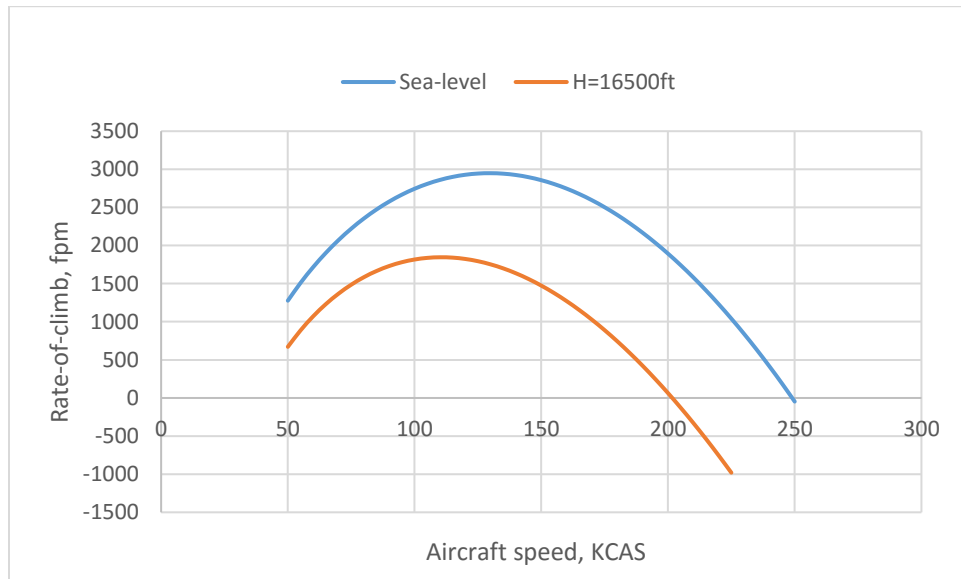


Figure 7.2.1. Climb performance for a 1000nmi mission weight with full payload

7.3. Cruise

Cruise performance can be described using Flight Envelope and Payload Range Curve. Cruise analysis considers for the 1000nmi mission with full payload. Flight envelope shown in Figure 7.3.1 relates minimum and maximum stall speeds with altitude. Iterative maximum level speed estimation based on an adjusted drag model was used to obtain maximum level speeds at different altitudes. Maximum speed of 254 KTAS can be reached at the sea level and increases up to 274 KTAS at the service ceiling. Cruise Stall speed at sea level equals 83 KTAS and increases with altitude until 123 KTAS.

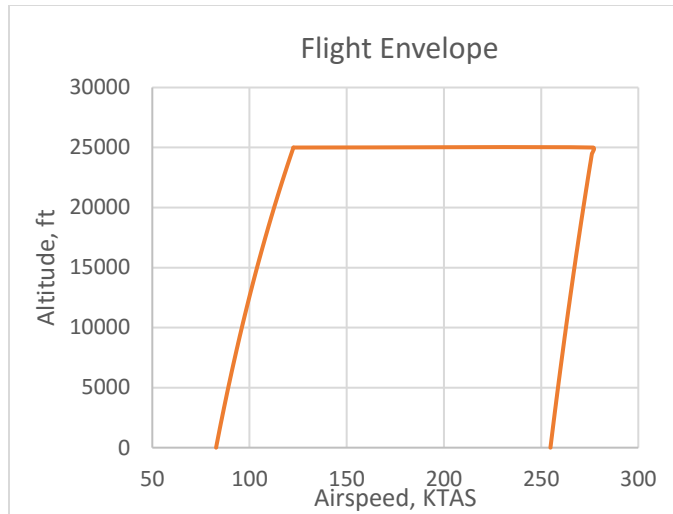


Figure 7.3.1. Flight Envelope

Payload Range Curve was obtained using Breguet range formula and is shown in Figure 7.3.2. Point zero shows maximum possible payload and no fuel. Point one presents maximum range of the aircraft with full payload, point two shows maximum range with full fuel tanks, and point three shows maximum range with no payload. All points on the payload diagram satisfy mission range requirements. In addition, maximum range substantially outperforms competitors of KR-1, which gives the aircraft bigger coverage area which is more beneficial for any aircraft.

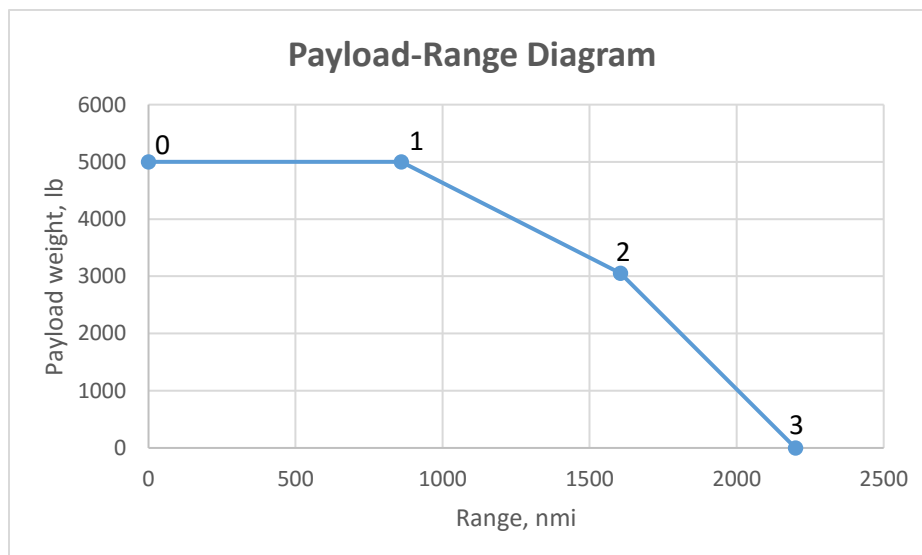


Figure 7.3.2. Payload Range Curve

Point	Payload Weight(lb)	Fuel Weight(lb)	Range (nmi)
0	5000	0	0
1	5000	4985	612
2	3050	6936	1605
3	0	6936	2150

Table 7.3.1. Payload, Range, and Range for critical points of the Payload Range Curve

7.4. Steady-state turn

Steady-state turn performance plays an important role in maneuverability of the aircraft. A more agile aircraft is capable of responding to different situations occurring during flight. Turn performance map is shown in Figure 7.4.1 and presents possible turning rates for particular turning speeds. Grey lines are load factor isolines showing load factor experienced by the aircraft at a particular turn rate and speed. Turn rates are constrained by limit load factor and stall that are shown as black and dashed blue lines respectively. Figure shows that maximum turn rate achieved at maximum possible turning speed equals to 17 degrees per second and equivalent to turn radius close to 1100 ft.

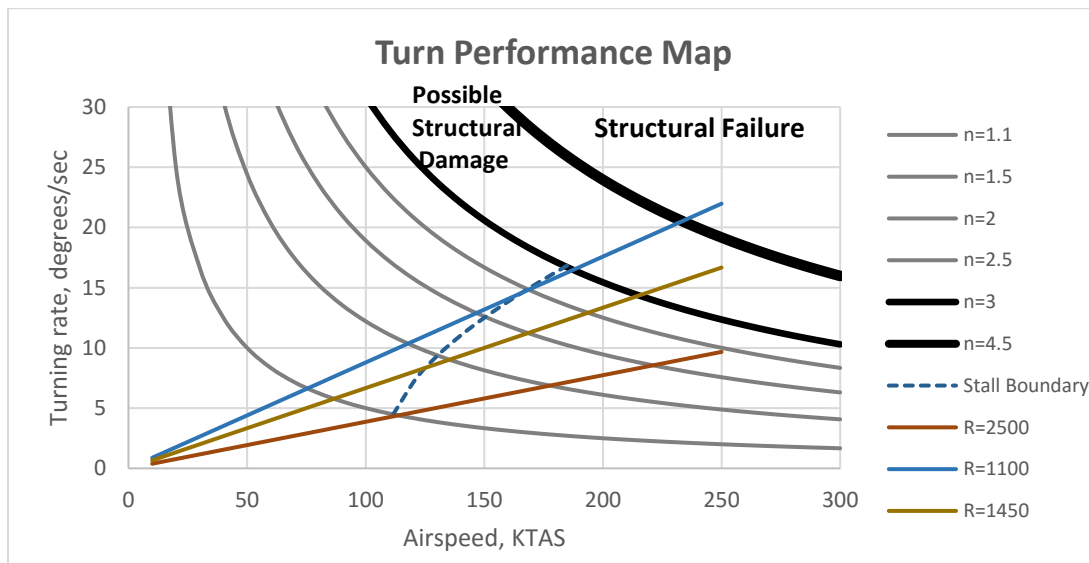


Figure 7.4.1. Turn Performance Map

7.5. Descent

Although descent performance may not seem to be crucial for the current design mission, an airplane with strong glide performance improves aircraft safety during an emergency, such as engine failure. Descent performance was analyzed for the 1000nmi mission with full passenger density at cruise altitude. Figure 7.5.1 shows descent performance of KR-1. Figure shows that maximum glide ratio occurs at the glide angle of -3.7 degrees with respect to the ground, and the aircraft has rate-of-descent of -980fpm at maximum glide ratio.

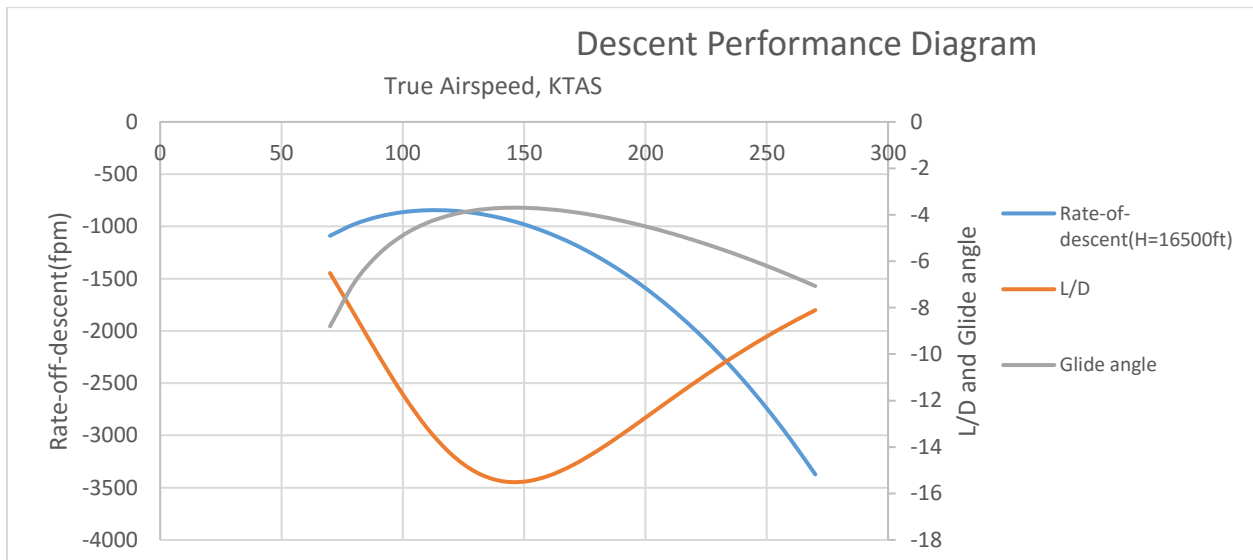


Figure 7.5.1. Descent Performance Diagram

8. Structures

8.1. V-n Diagram

To successfully design structure of the airplane, and perform required calculation, first, a V-n diagram must be obtained. V-n diagram was developed using FAR Part 25 load requirements. Minimum ultimate positive load factor was estimated to be 2.87, but is decided to be increased up to 3, while negative factor was -1.5, considering typical transport aircraft load factors from Raymer [2]. Gust speeds of 25ft/s and 50ft/s were also considered using estimations from FAR Part 25 requirements. After design cruise speed is reached, positive load factor begins to decrease until reaches value of two at the dive speed. This decision was made to decrease maximum possible loads developed by the structure and decrease structural weight [11]. Figure

8.1.1-8.1.3 show the V-n diagrams with stall speeds at sea level, cruise altitude, and service ceiling.

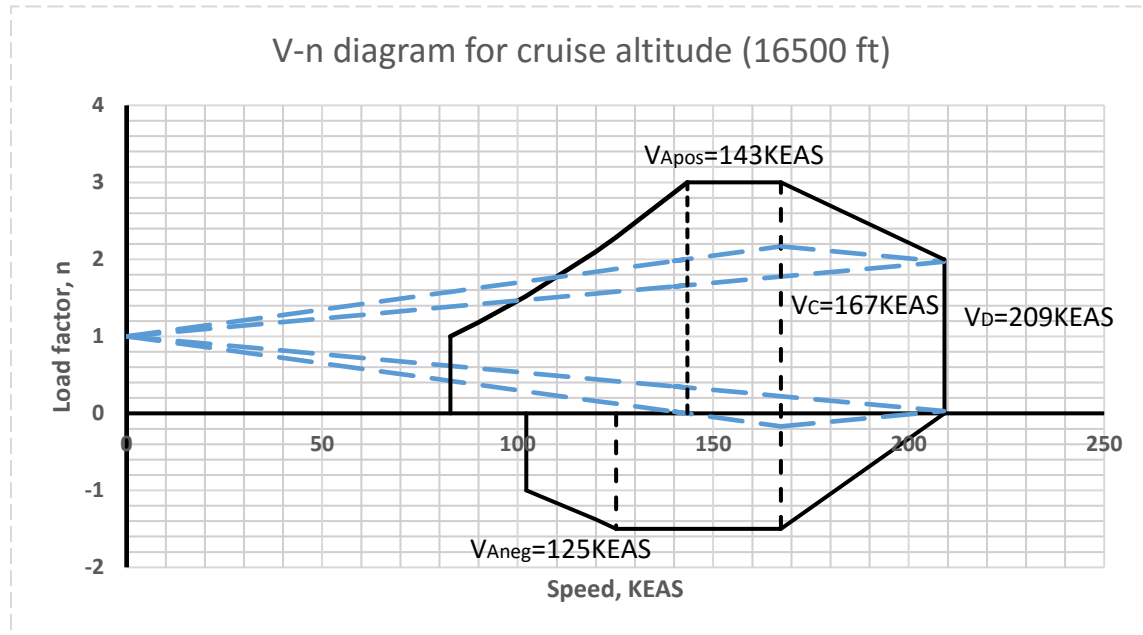


Figure 8.1.1. V-n Diagram at cruise altitude

8.2. Material selection

Material selection plays an important role in structural behavior of the aircraft, its weight, and cost related to both manufacturing and maintenance. For the given RFP, aluminum was used as the main material due to its low cost, predictable strength capabilities, and ease of certification. For major parts of the structural analysis, Aluminum 2024-T4 was used because of its high strength and weight combination. Table 8.2.1 shows material properties of Aluminum 2024-T4.

Density (lb/in ³)	0.1
Ultimate Tensile Strength (ksi)	62.0
Yield Strength (ksi)	40.0
Young's Modulus (10 ⁶ psi)	10.5
Shear Modulus (10 ⁶ psi)	4.1

Table 8.2.1. Aluminum 2024-T4 material properties [12]

8.3. Wing and tail structure

Loads experienced by the wing structure was obtained using advanced beam method presented in Allen [14] and Megson [15]. Loads for internal forces and moments were first approximated using Schrenk's approximation, and results from OpenVSP were used for later iterations. Aircraft maximum cruise speed at cruise altitude with maximum load factor was used to calculate internal forces and moments. Maximum sideslip angle for the aircraft was assumed 12 degrees to calculate the loads on the vertical tail. Figure 8.3.1 shows a coordinate system used for forces and moments calculations in the wing and empennage. Figures 8.3.2-8.3.4 show shear force bending moment distributions along the wing and the tails.

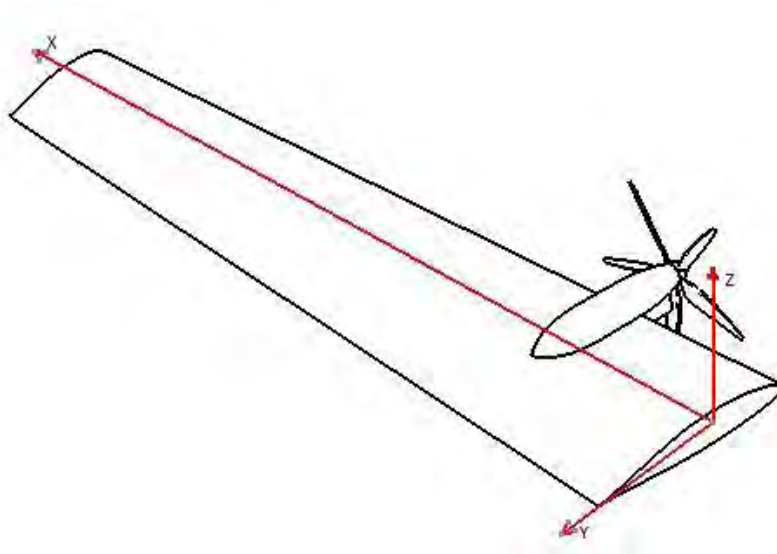


Figure 8.3.1. Wing coordinate system used for structural analysis

Safety factor of 1.5 was applied to design the structure of the aircraft. To determine the best location of the main and rear spars of the wing and the tails, several constraints were applied. First, positioning of the spars was constrained due to the presence of the lifting and control surfaces and fuel tanks in the wing. The constraint of 25% chord in the wing for the main spar and 70% for the rear spar were determined based on fuel tanks arrangements. As long as the thickest part of the spar, considering constraints, occurs at 25% chord, the main spar was put there because thicker spar would withstand higher bending stresses, so weight

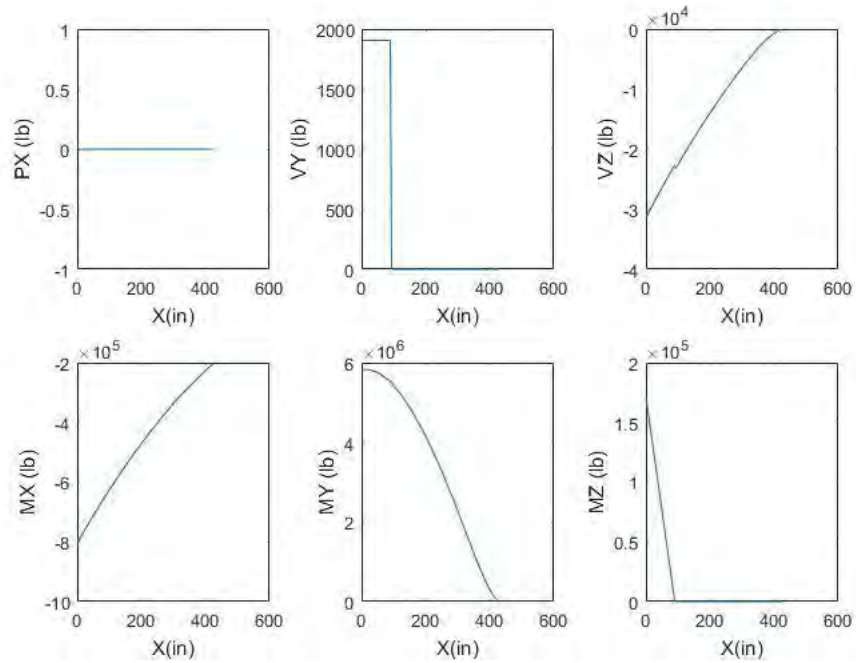


Figure 8.3.2. Internal forces and moments experienced by the wing. V=215KTAS, H=16500ft, n=3.

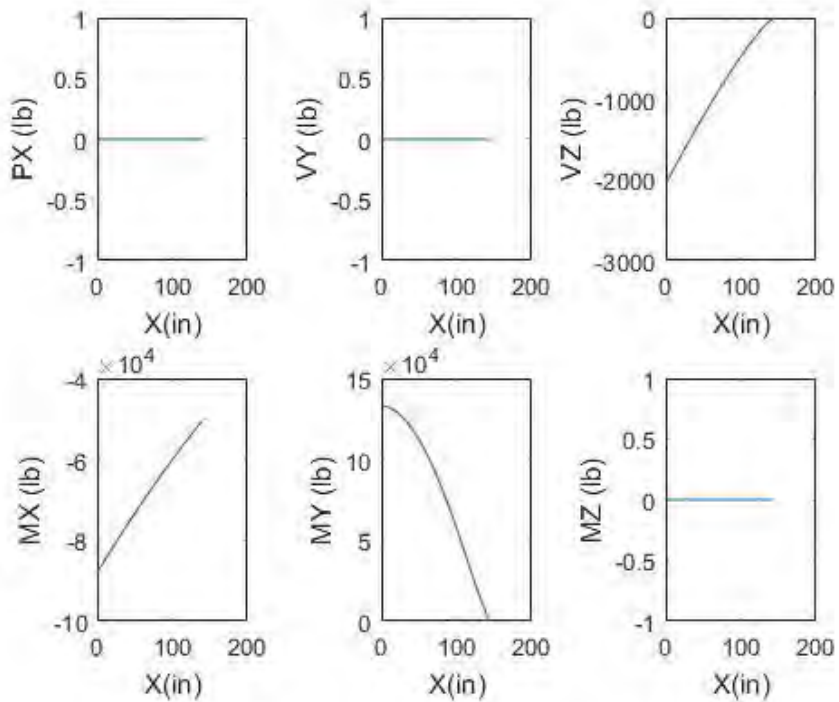


Figure 8.3.3. Internal forces and moments experienced by the H-tail. V=215KTAS, H=16500ft, n=3.

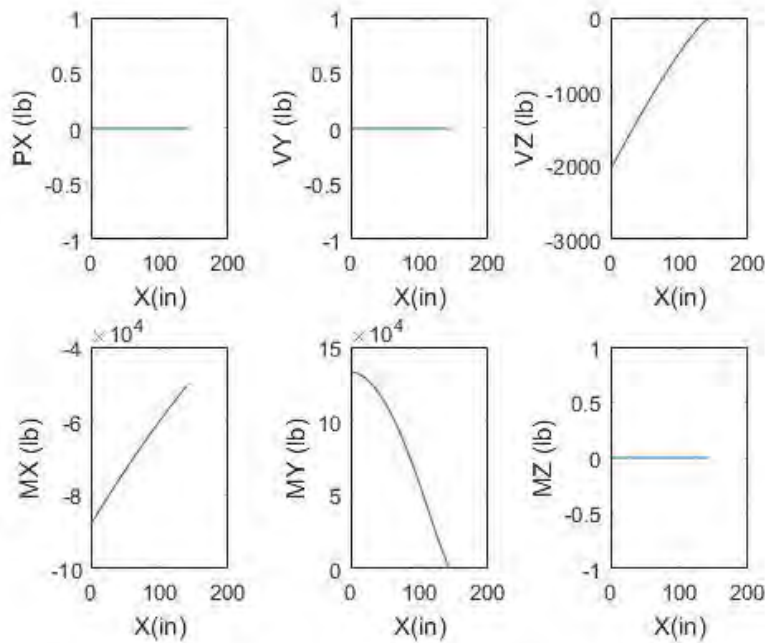


Figure 8.3.4. Internal forces and moments experienced by the H-tail. V=215KTAS, H=16500ft, n=3.

can be saved. The rear spar was put to 70% chord due to the flap attachment. In addition, twenty stringers were located uniformly along the wingbox to help withstand bending stresses. Main spars for the horizontal and vertical tails were put close to the thickest point of the airfoil section at 27% and 23% respectively. Rear spars was located close to the control surfaces: at 30% chord for both tails. All spars are tapered along the span. Figures 8.3.5-8.3.7 show dimensions of the spars for the wing and the empennage. Skin thickness of 0.025in was used for the wing and vertical tail while 0.05in thick skin was put on the horizontal tail. Ribs were located using Euler buckling formula as a preliminary method with larger amount of ribs being close to the root and steadily decreasing amount towards the tip. A MATLAB script was developed based on methods of Allen to find modulus-weighted centroids of each wing section and investigate bending and shear stresses along the span. In addition, the script calculates preliminary weight of the structure base on material properties input. Root locations of structural components are input from Excel into MATLAB, and the script calculates all properties along the span. In addition, the code features an option of analysis of strutted wing to investigate structural behavior of the airplane and estimate the weight. Results regarding

trade study between a cantilever and strutted wings are shown in Section 2. Figures 8.3.8 and 8.3.9 show the structural layout of the wing and the empennage.

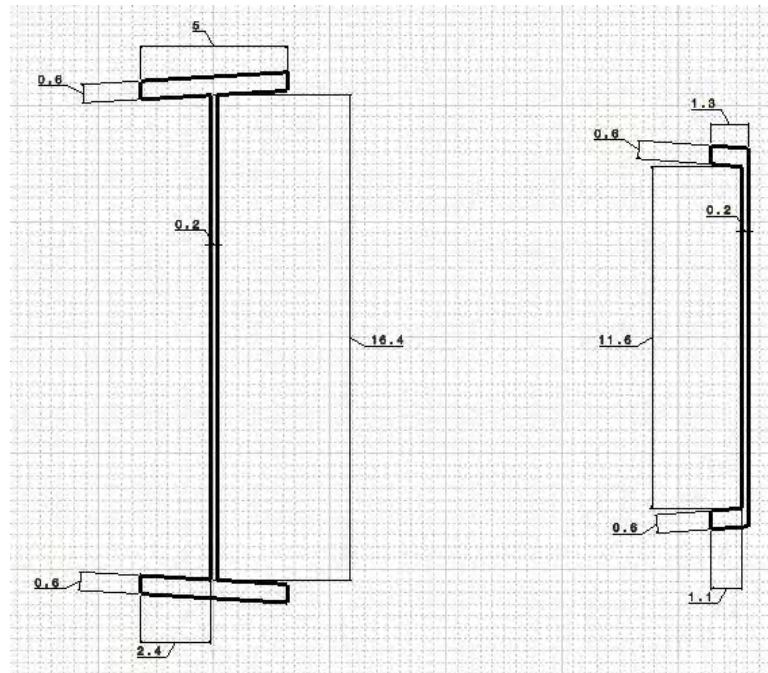


Figure 8.3.5. Wing Front and rear spar dimensions

Fuselage structure was estimated based on a number of simplification assumptions: weights of aircraft components were assumed as point masses and analysis would be done on the section with maximum internal forces and moments experienced. Figure 8.2.10 presents shear and moment diagrams of the fuselage. Loads with load factor of 3 were considered for the fuselage analysis. A structure of the fuselage is composed of the skin and 24 stringers to withstand the loads. Figure 8.2.11 shows the 2_D layout of the fuselage stringers. Shear and buckling analysis of must also be perform to determine locations of fuselage ribs and skin thickness. In addition, more accurate analysis using more advanced approximations such as Finite Element Analysis needs to be done.

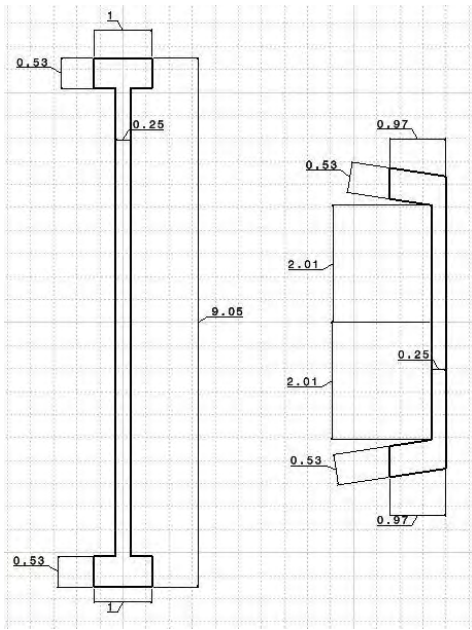


Figure 8.3.6. Horizontal tail spars dimensions

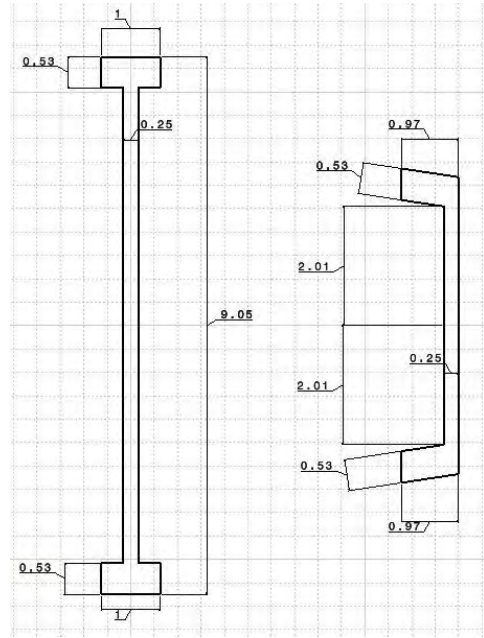


Figure 8.3.7. Vertical tail spars dimensions

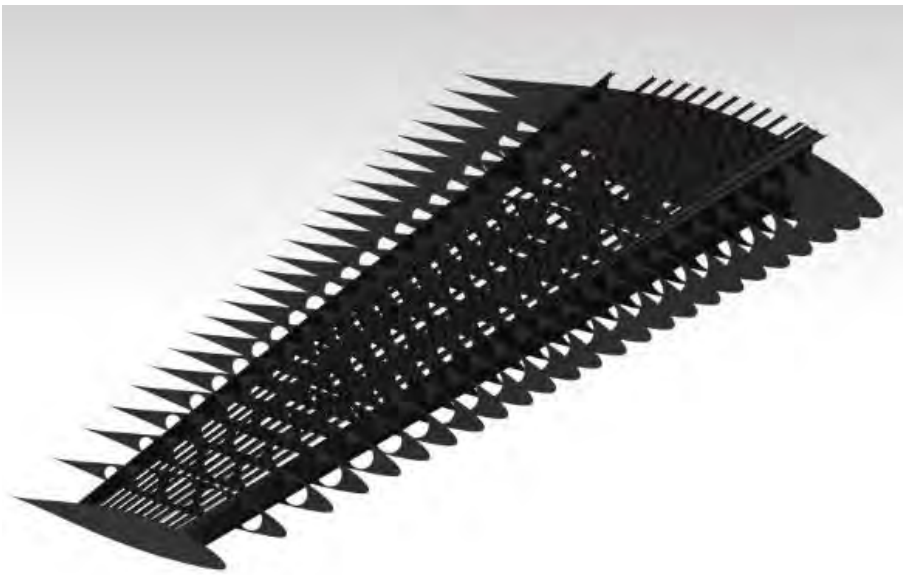


Figure 8.3.8. Wing structural layout

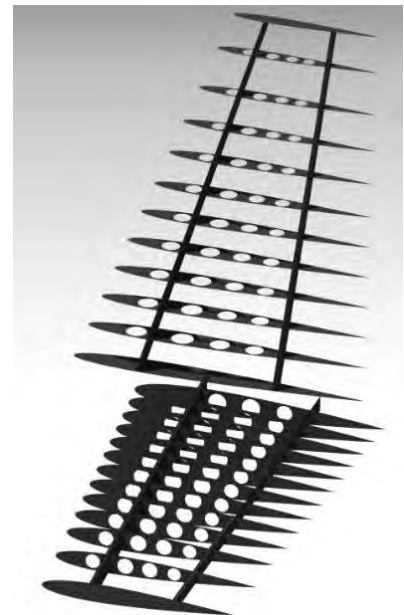


Figure 8.3.9. Empennage structural layout

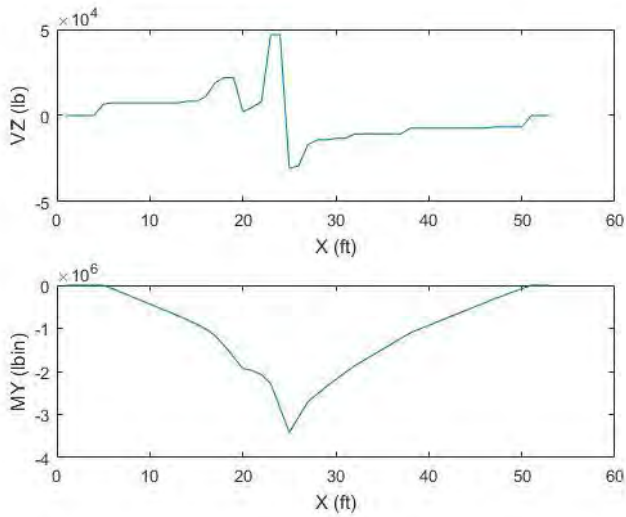


Figure 8.3.10. Shear and Moment diagrams of the fuselage

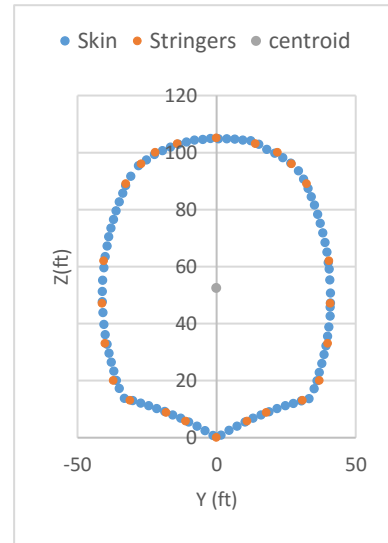


Figure 8.3.11. Stringers layout

9. Stability and Control

To ensure adequate aircraft performance and safety, the aircraft must be statically and dynamically stable, controllable, and have appropriate handling qualities specified by MIL Specs, so the empennage and aircraft control surfaces must be properly sized.

9.1. Static stability and control analysis

Static stability analysis was performed using classical theoretical approach from Raymer [2], Nelson [14], and Gudmundsson [3]. Aircraft must be statically stable at all operating airspeeds and cover as large cg range as possible without major losses in controllability.

Horizontal tail was initially sized using historical data from Raymer [4] and was modified later for the mission requirements. Figure 9.1.1 shows the horizontal tail layout and elevator sizing, and Table 9.1.1 shows horizontal tail parameters and dimensions. The elevator was sized such that a combination of elevator power and losses due to large possible elevator deflections are balanced. Using DATCOM experimental data, 30% chord elevator was used along 85% percent of the elevator span.

Aspect ratio	4.36
Horizontal tail volume ratio	0.83
Span	24 ft
Root chord	6.25 ft
Taper ratio	0.75

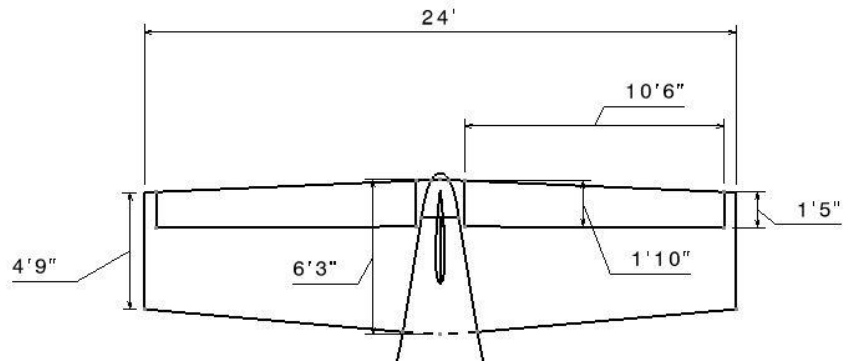


Table 9.1.1. Horizontal tail parameters

Figure 9.1.1. Horizontal tail layout

In addition, vertical location of the horizontal tail plays an important role in stall recovery. Horizontal tail should not be blanked by the wake produced by the wing at high angles of attack. Figure 9.1.2. shows different tail locations and their acceptability in terms of stall safety. Horizontal tail on KR-1 was put 1 ft below the wing level to not to interfere with the horizontal tail in case of rudder and elevator being deflected simultaneously. Such location does not put the horizontal tail into the blanked zone.

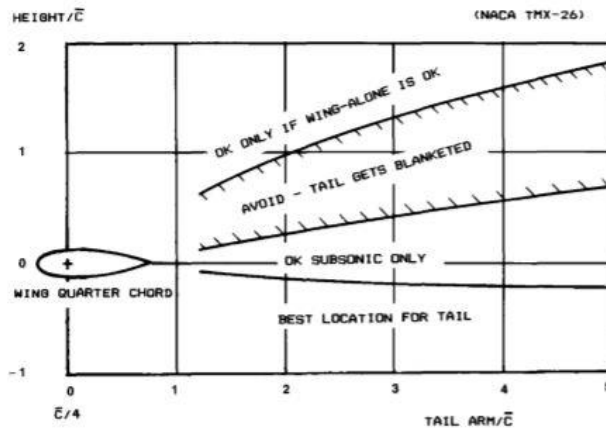


Figure 9.1.2. Horizontal vertical location diagram [2]

Vertical tail was sized based on requirements of the engine-out case at low speeds. Specified by FAR Part 25: minimum control speed may not exceed $1.13 V_{SR}$. Figure 9.1.3 show the free-body diagram of the forces and moments produced by the aircraft with one engine inoperative. The vertical tail must withstand

moments produced by the operating engine and windmilling propeller. In addition, size of the tail should not be excessive to minimize drag and weight. After multiple iterations, a good compromise of size and functionality was achieved. Figure 9.1.4 shows the vertical tail layout, and Table 9.1.2 shows vertical tail parameters and dimensions. Maximum rudder deflection required to trim the aircraft in case of one engine inoperative is equal to 22° which if is acceptable for a simple flap in terms of flow separation (Maximum deflection of 25° is considered to be maximum for a simple flap) [3].

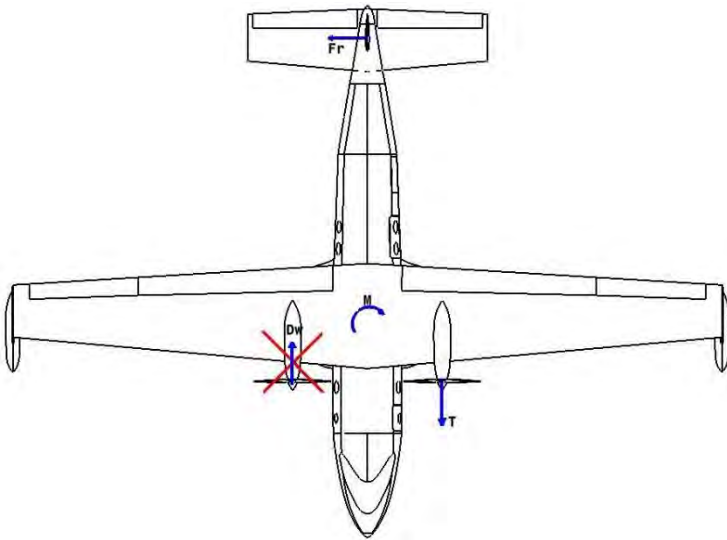


Figure 9.1.3. Engine-out case free-body diagram

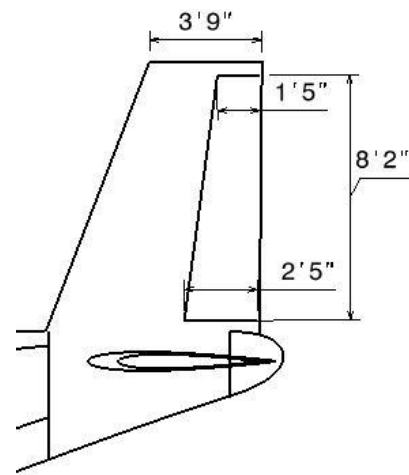


Figure 9.1.4. Vertical tail layout

The location of the vertical tail with respect to the horizontal tail becomes important in case of spin recovery. At least 30% of the rudder should be away from the horizontal tail wake to ensure vertical tail control characteristics. However, preliminary location of the horizontal and vertical tails enable only 11% of the rudder. To improve flow characteristics at the vertical tail at high angles of attack and increase efficiency of the rudder, a dorsal fin was used. However, the dorsal fin does not guarantee better behavior of the flow at high angles of attack. More care must be taken to reach appropriate percent of rudder unblanked. Figure 9.1.5 shows the wake blockage diagram.

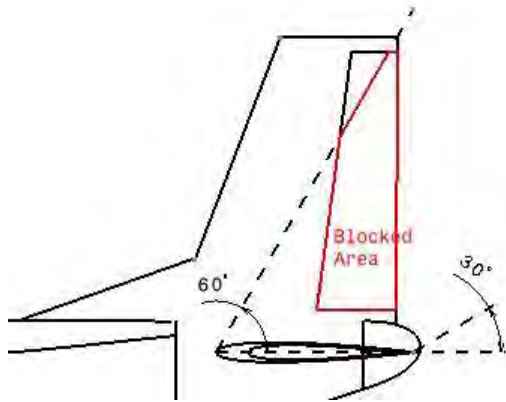


Figure 9.1.5. Wake blockage diagram

Aspect ratio	1.82
Vertical tail volume ratio	0.036
Span	10 ft
Root chord	7.33 ft
Taper ratio	0.5

Table 9.1.2. Vertical tail parameters

To satisfy turning performance specified by FAR Part 25 of the aircraft, ailerons must be properly sized. However, aileron sizing is constrained by the flaps used to satisfy take-off requirements. Roll rate estimation was done using Sadraey [8] and compared to MIL-STD Category B Class 2 requirements. Maximum aileron deflection was assumed to be 20° . Table 9.1.3 shows comparison between calculations and requirements and Figure 9.1.6. shows the aileron layout.

	Time to achieve a bank angle of 45° (s)
Sadraey	1.12
MIL-STD Category B Class 2	1.90

Table 9.1.3. Roll rate requirements comparison

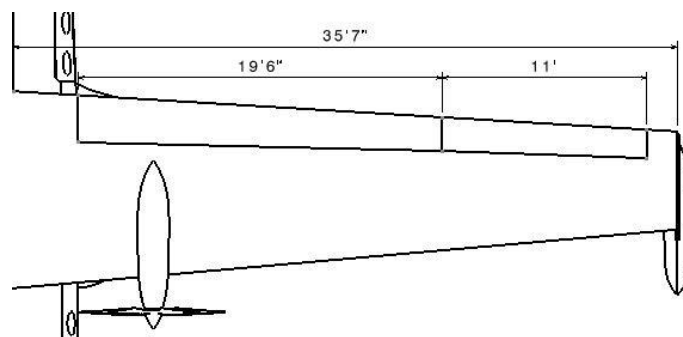


Figure 9.1.6. Aileron layout

Table 9.1.4. shows final static stability and control derivatives. Data shows that the aircraft is statically stable.

Coefficient	Value
CM_{α}	-0.575
CM_q	-21.127
CY_{β}	2.415
Cn_{β}	0.116
$Cn_{\delta r}$	-0.120
$Cn_{\delta a}$	-0.017
Cl_{β}	-0.088
Cl_p	0.236
$Cl_{\delta r}$	0.022

Table 9.1.4. Static stability coefficients

9.2. Dynamic stability analysis and handling qualities

Any aircraft should satisfy dynamic stability and control requirements. Matlab/Simulink model called

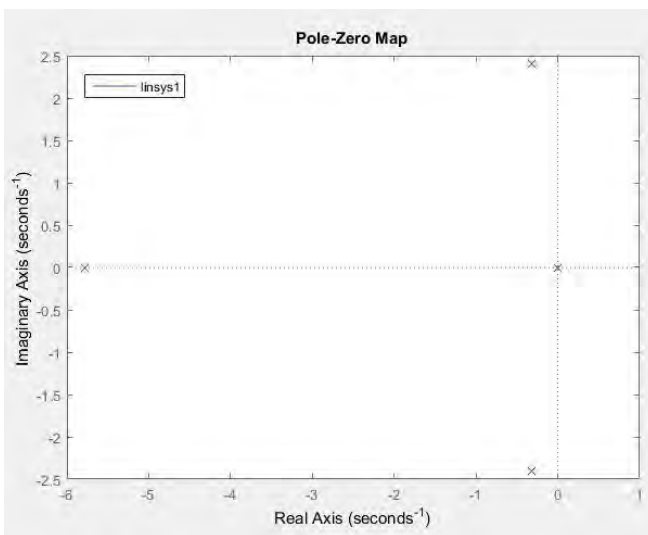


Figure 9.2.1. Longitudinal motion poles and zeros

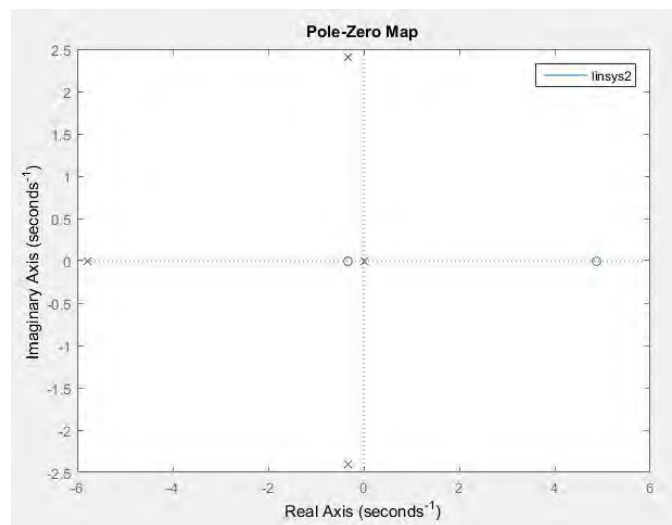


Figure 9.2.2. Lateral motion poles and zeros

NAVION developed at Embry-Riddle Aeronautical University was used to perform dynamic stability analysis. Figures 9.2.1 and 9.2.2 show roots of the transfer function obtained for a linearized 6 DOF model. Roots located at the zero indicated navigational states that do not depend on anything, so they are not required for the analysis. Other zeros show that the aircraft is dynamically stable.

In addition, handling qualities play an important role in the aircraft design. Results obtained for cruise speed at cruise altitude were compared to MIL-STD Category B requirements [17] [18]. Table 9.2.1. shows results obtained from the NAVION model. All values satisfy Level 1 requirements that are desired. However, dynamic stability analysis must be performed for a range of airspeeds to ensure good handling qualities for all sections of flight.

Mode		MIL-STD Cat. B Level 1 Requirements	KR-1
Short Period	Damping	$0.30 < \zeta_{SP} < 2.00$	0.48
	Natural frequency (rad/s)	$1.10 < \omega_{NSP} < 6.00$	3.89
Phugoid	Damping	$\zeta_{PH} > 0.04$	0.144
Dutch Roll	Damping	$\zeta_{DR} > 0.08$	0.13
	Natural frequency (rad/s)	$\omega_{NSP} < 4.00$	2.42

Table 9.2.1. Dynamic stability analysis of KR-1

10. Aircraft systems and layout

10.1. Landing gear

Landing gear required for the RFP must provide the aircraft successfully perform on different runways and be as small and light as possible.

Tricycle landing gear was chosen for the present design as one of the most commonly used type of the landing gear for transport aircraft.

Longitudinal and lateral positioning of the landing gear determines the ability of the aircraft to rotate during take-off and maneuver on the ground. Nose landing gear should not carry more than 20% of MTOW with the cg being at the forward limit, and no less than 10% when the cg is at the aft limit. Table 10.1.1 summarizes the percent of the MTOW experienced by the aircraft at the most forward and aft positions.

CG location	Percent MTOW
Most Forward	18%
Most Aft	12%

Table 10.1.1. Percent MTOW experienced by the nose landing gear at cg limits

The main landing gear should be located such that the aircraft can rotate up to maximum angle of attack to prevent tail strikes. In addition, the main gear should be offset behind the most aft cg such that the angle between the vertical line through the gear and the line crossing the gear and the cg must be equal to the

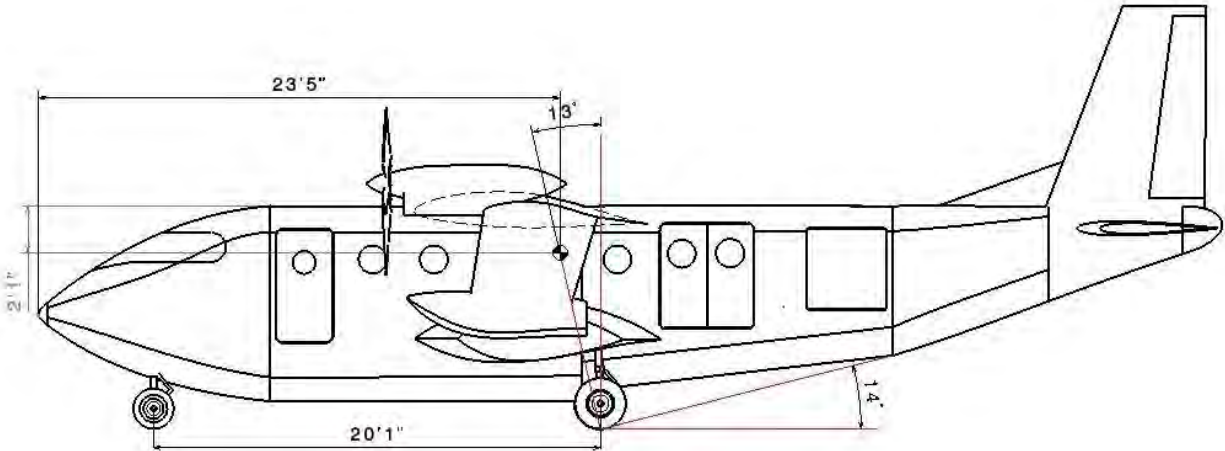


Figure 10.1.1. Longitudinal landing gear location

maximum possible rotation angle. Figure 10.1.1 presents the diagram of the longitudinal landing gear location.

Wheel track of the main landing gear determines whether the aircraft is stable while turning and taxiing. The wheel track, the height of the gear, and the distance between the nose gear and the main gear should be estimated such that the angle shown in Figure 10.1.2 should be less than 63° . The Figure demonstrates that the angle meets the requirements; however, a compromise between the landing gear positioning and the aircraft aerodynamics was made. Due to the size of the landing gear and the tires discussed below, the main landing gear was put in the fuselage and additional extended fuselage sections were designed to fit the landing gear. These sections, however, increase drag, so decrease aerodynamic efficiency of the aircraft. The retraction mechanics of the landing gear is shown in Figure 10.1.3.

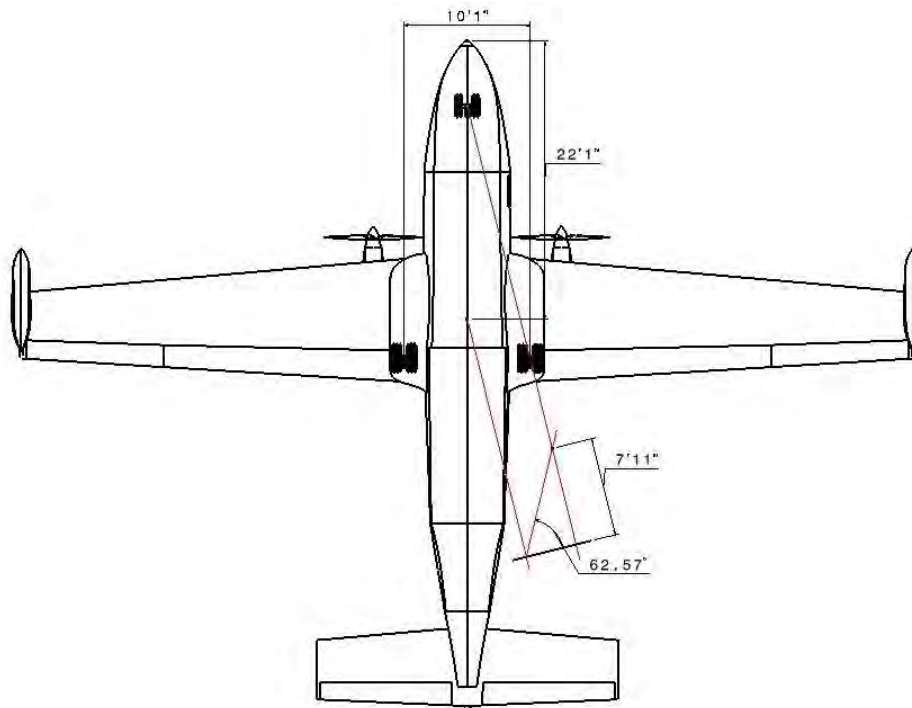


Figure 10.1.2. Lateral landing gear location

Tires play an important role in aircraft abilities to take-off from different surfaces. Low-pressure tires are desired to take-off from soft and wet profiles, so 60 psi tires were considered for the current design. Weight experienced by the tires assumes the most aft cg for the main gear and most forward cg for the most forward cg as well as 25% weight increase due to historical tendency of aircraft weight increase in time. Goodyear aviation database [19] was used to find appropriate tires that can withstand the loads applied by the aircraft and have low-pressure rating. Table 10.1.2 shows information regarding the tires used. More information regarding tires can be found in Reference 17.

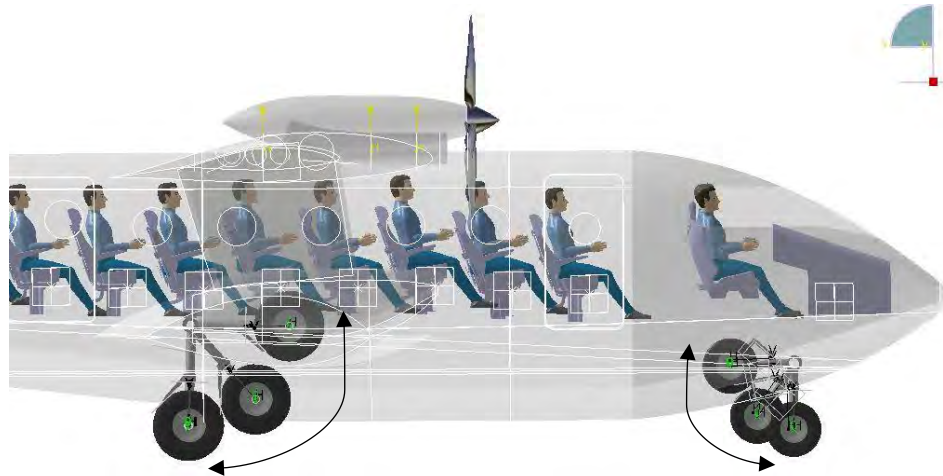


Figure 10.1.3. Landing gear retraction

	Main	Nose
Trademark	Flight Leader	Flight Custom 3
Part number	922C86T1	650T66-3
Number of tires	2	2
Size	9.25-12	6.5-10
Ply rating	8	6
TT or TL	TL	TL
Rated speed (mph)	160	160
Rated Load (lb)	5600	2770
Rated inflation (psi)	60	60
Maximum breaking load (lb)	8120	4020
Maximum breaking load (lb)	15100	7500

Table 10.1.2. Tires specs used for KR-1 landing gear [19]

Oleo-pneumatic landing gear was used for the KR-1 as the system which has shock absorber features that are useful for hard landing and operation on rough surfaces. In addition, the gear itself does not have inclination with respect to the ground and no castering was used for the wheels, so the nose wheels are neutrally stable both statically and dynamically. Figure 10.1.3 shows the layout of the landing gear.



Figure 10.1.3. Landing gear layout

10.2. Cabin pressurization and air conditioning

Due to operational altitude of 16500ft and service ceiling of 25000ft, cabin pressurization and air conditioning system is required to ensure safe and comfortable flight of both the crew and passengers. The air is transported from the turboprop engines compressors to the cabin where it is distributed in the fuselage and cooled down in the AC system.

10.3. Fuel system

Four fuel tanks are located in the aircraft wing between the main and rear spars. The tanks are separated by the center section of the aircraft and two engines. Maximum fuel volume is 1024 gal. JET-A1 fuel was chosen for the current aircraft as a high-quality fuel, and fuel density of 6.7 lb/gal was used for all calculations. Purple section in Figure 10.3.1 shows the layout of the fuel system inside the wing.

10.4. Fuselage layout

The passenger cabin and its doors are substantially elevated relative to the hull bottom to enable boarding and cargo loading for the aircraft being on the water, so the doors have enough clearance comparing to the waterline. The cabin was designed for 20 passengers and one cabin crewmember. The crewmember has a separate row close to one of two exits. The aft exit has double doors to quickly load heavy and irregular cargo for the cargo configuration of the aircraft. To easily distribute cargo in the cabin, integrated roller system was included in the cabin. For the passenger configuration, the rows near the aft door are arranged such that passenger

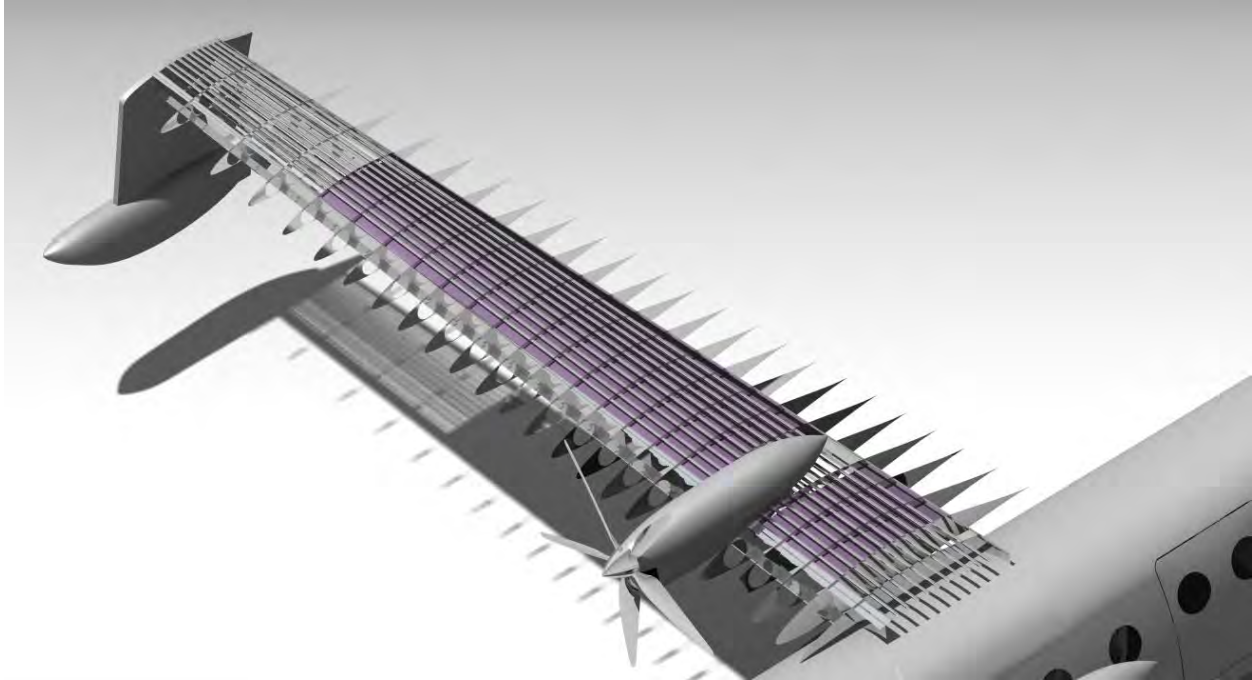


Figure 10.3.1. Fuel tank layout

have enough room to maneuver while entering or exiting the aircraft. Seat pitch in the cabin is equal to 30 inches that satisfies the RFP requirement and has more extra space for more comfort. The seats are designed for a 95-percentile passenger to cover the majority of passenger types. The aisle width is equal to 13 inches to give enough room for the passengers to move during boarding or emergency situation. Figures 10.4.1-10.4.3 show the cabin dimensions and Figure 10.4.4 demonstrates doors dimensions. Cargo configuration option is presented in Figure 10.4.5.

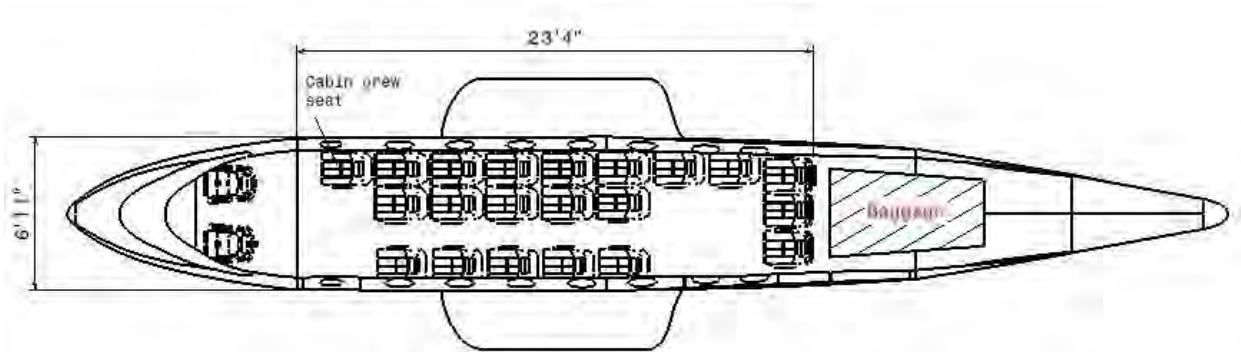


Figure 10.4.1. Cabin top view

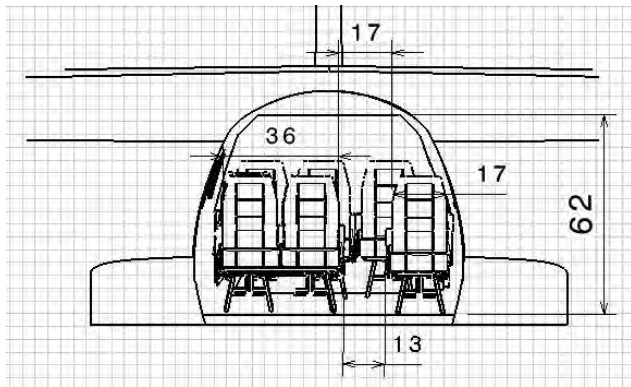


Figure 10.4.2. Cabin front view

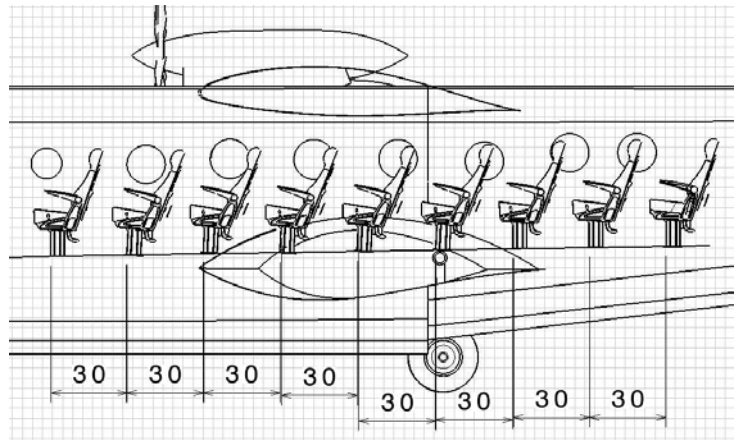


Figure 10.4.3. Seat pitch

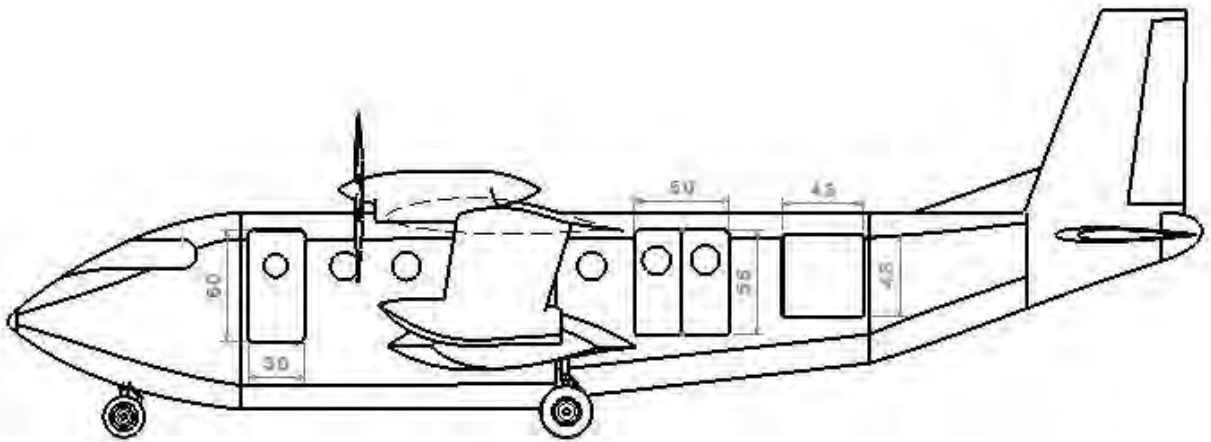


Figure 10.4.4. Doors dimensions

Baggage of KR-1 is located behind the cabin and has available volume of 87ft^3 which satisfies the RFP. A side door is designed to have access to the baggage section. Figure 10.4.6 shows the baggage layout.

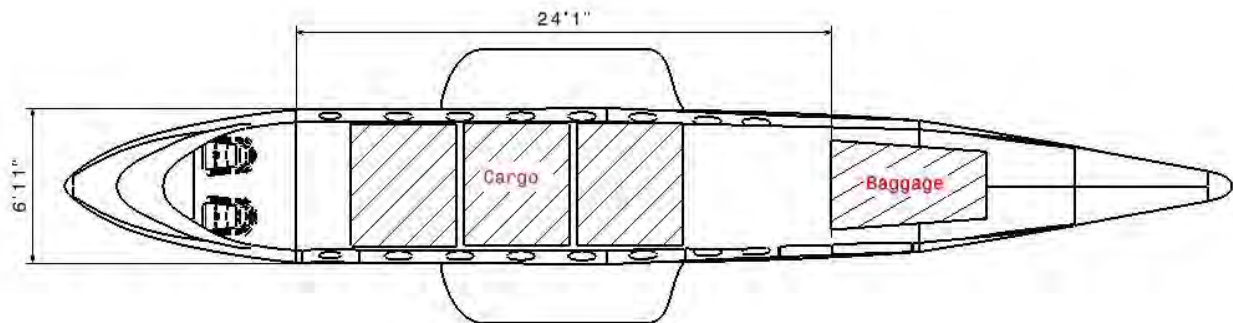


Figure 10.4.5. KR-1 cargo configuration

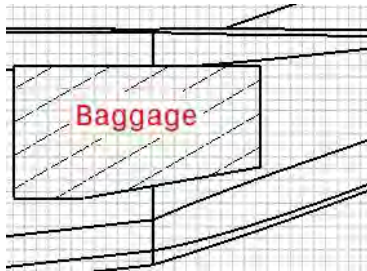


Figure 10.4.6. Baggage compartment side view

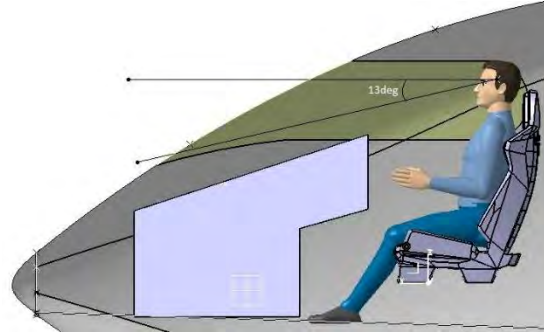


Figure 10.4.7. Cockpit view

For the cockpit, the pilot location and the windshield was designed such that the pilots have sufficient visibility to operate the aircraft. Pilot visibility angle is shown in Figure 10.4.7, and the angle of 13° satisfies common practice for transport aircraft.

10.5. Anti-icing system

Anti-icing system is located in the wing leading edge along the whole span for both vertical and horizontal tails to ensure safe operation and prevent fatal flow separation. Figure 10.5.1 shows the cross-section of the anti-icing system and orange sections in Figure 10.5.2 present its location in the aircraft.

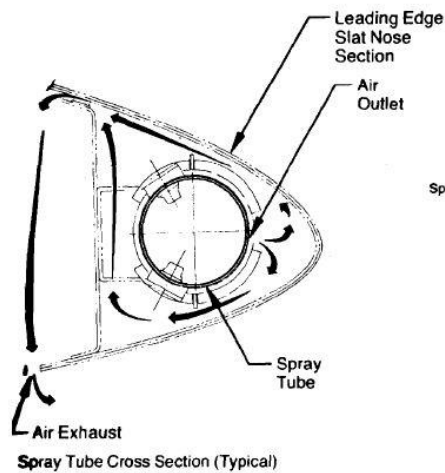


Figure 10.5.1. Anti-icing cross-section [20]



Figure 10.5.2. Anti-icing system layout

11. Cost analysis

Cost analysis determines whether the aircraft will be competitive in the market and how fast is possible to begin getting profit from aircraft manufacturing and selling. The cheapest possible aircraft is desired considering constraints.

According to RFP, KR-1 shall be available by 2027, so the aircraft cost must be inflated using the following relation

$$C_i = 1.031^{\text{inflated year} - \text{current year}} C_c$$

Where C_i is the inflated cost and C_c is the cost of the year of analysis.

11.1 Fuel economy

Fuel economy plays an important role in potential success of the aircraft: the less fuel is required per seat, the cheaper the flight, so more demand will be for the particular airplane. Based on RFP, the designed airplane must demonstrate at least 20% reduction in fuel burn per passenger on a similar mission length.

To compare the fuel economy results, three aircraft on a 300nmi mission were considered: Beechcraft 1900D [21], Dornier 228 [22], and DHC-6 Twin Otter [23]. Based on preliminary design sizing and performance, fuel economy of KR-1 was calculated based on the passenger weight specified in RFP and compared to two baseline aircraft. Table 11.1.1 shows the fuel economy results.

Aircraft name	Fuel per seat (miles per gal)
Beechcraft 1900D	35.8
Dornier 228	37.8
DHC-6 Twin Otter	34.6
KR-1	34.3

Table 11.1.1. Fuel economy comparison

Results show that KR-1 demonstrates similar fuel economy comparing to existing aircraft, however it does not outperform them by 20%. Possible solution may be to reduce the aircraft weight by introduction of

composite materials and modifications of the wing geometry to increase the glide ratio, so fuel-to-weight ratio may be reduced and less fuel will be required for the mission to be completed.

11.2 Research, Development, Testing, and Evaluation

Eastlake model was used to estimate the aircraft development cost in 2027 U.S. dollars. Table 11.2.1 shows rates for all necessary labors to develop and manufacture the aircraft. The total cost of production including the manufacturer’s liability insurance of \$50 thousand is equal to \$9.77 million. Figure 11.2.1 shows the production cost breakdown.

Engineering	90 \$/hr
Tooling	60 \$/hr
Manufacturing	50 \$/hr

Table 11.2.1. Rates for aircraft development

Assuming to be able to produce 250 aircraft in 5 years and have a unit price of \$9.9 million in 2027, it will take 245 aircraft to reach the breakeven point. Figure 11.2.2 shows the breakeven analysis results.

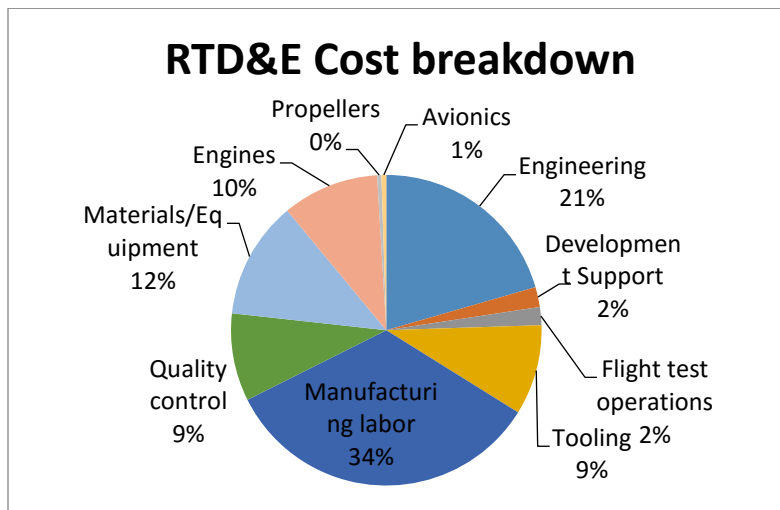


Figure 11.2.1. RTD&E Cost breakdown

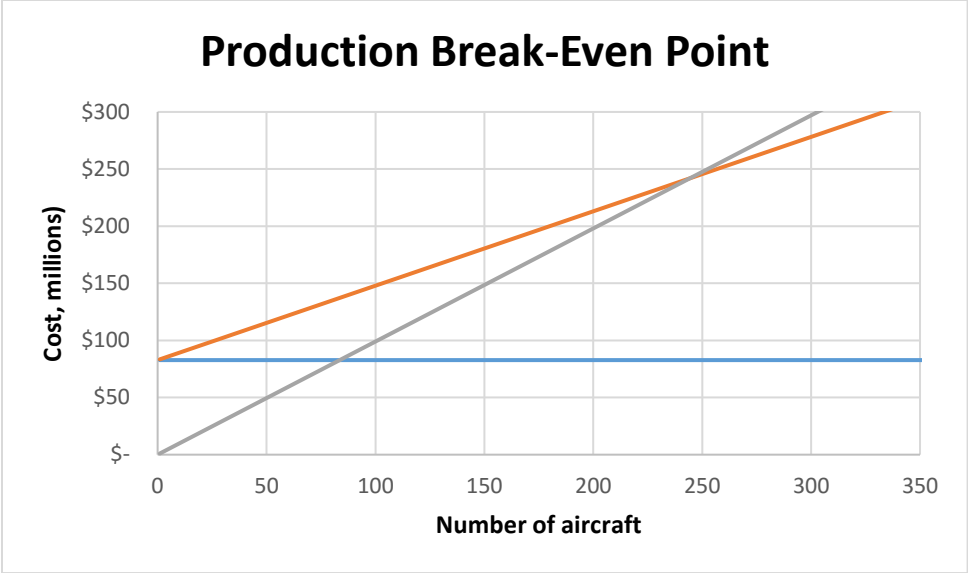


Figure 11.2.2. production breakeven point (Eastlake Model)

11.3. Operational Costs

The operational cost was calculated using the method provided by Gudmundsson. The calculation assumed 500 flight hours per year, 85% thrust at cruise altitude, storage rate of \$1000 per year, JET-A1 fuel cost of \$5.2/gal, insurance cost of \$8000, and crew rate of \$100/hr. The total operational annual cost becomes \$816 thousand. Figure 11.3.1 shows the operational cost breakdown.

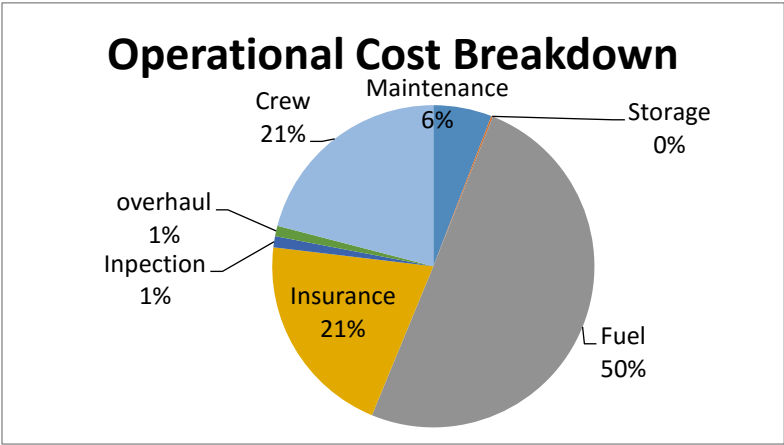


Figure 11.3.1. Operational cost breakdown

12. Compliance Matrix

Number	Requirement Description	Met (Y/N)	Reference
1	Take off and land from different runways	Y	Landing gear design
2	Take-off and land from fresh and salt water	Y	Take-off and landing analysis
3	Minimum cruise speed of 200 knots (250 desired)	Y	Flight envelope
4	Anti-icing system	Y	Anti-icing system
5	Fuel burn at least 20% better than existing aircraft	N	Fuel economy
6	Ground STOL within 1500ft over a 50ft obstacle for a 250 nmi mission at SL	Y	Take-off and landing analysis
7	Water STOL within 1900ft over a 50ft obstacle for a 250 nmi mission at 5000 ft	Y	Take-off and landing analysis
8	1000 nmi range for full passenger density	Y	Cruise analysis
9	500 nmi range with 5000lb cargo	Y	Cruise analysis
10	Ability to unload, refuel, and load cargo in no more than 60 min	Y	Fuselage layout
11	Ability to carry odd shaped cargo or a standard container	Y	Fuselage layout
12	Meet FAA 14 CFR Part 25 rules	Y	

13. Conclusion

KR-1 concept was picked out of four different configurations that represent current industry of amphibious transport aircraft. The aircraft is capable to complete all required missions specified by RFP and capable of

having two configurations: passenger version and a transport variant. Passenger version has 20 seats with one extra seat for a cabin crew. The transport version has a capability of carrying irregular cargo shapes and has a layout which makes reloading quick and easy. Performance parameters show superior capabilities of KR-1 comparing to current aircraft. However, fuel economy per seat does not show substantial improvement required by the RFP.

Overall, the aircraft should be a strong alternative to existing airplanes for medium-range missions with different airports of different quality. The aircraft should enter the market by 2027.

References

- [1] “IHS Jane’s all world aircraft, Development and production”, Coulsdon
- [2] Beriev aircraft official web-site, http://www.beriev.com/eng/Be-112_e/be-112_e.html
- [3] S. Gudmundsson, “General Aviation Aircraft Design: Applied Methods and Procedures”. Butterworth-Heinemann, Oxford, 2013.
- [4] D. Raymer, “Aircraft Design: A Conceptual Approach 5th edition”, AIAA, Washington, D.C., 2012.
- [5] D. Soban, “AE 3310 Performance Lecture notes”, Georgia Institute of Technology.
- [6] I. Abbott, A. von Doenhoff, “Theory of Wing Section: Including a Summary of Airfoil Data”, Dover Publications, New York, 1959.
- [7] E. Torenbeek, “Synthesis of Subsonic Airplane Design, 2nd Edition”, Delft University Press, 1982.
- [8] M. Sadraey, “Aircraft Design: a system engineering approach”, Willey, Chichester, West Sussex, UK, 2013.
- [9] L. Nicolai, “Fundamentals of Aircraft and Airship Design. Vol 1’, AIAA, Reston, VA, 2010.

- [10] CRF FAR Part 25 Electronic Code of Federal Regulations, https://www.ecfr.gov/cgi-bin/retrieveECFR?gp=&SID=0b32ac96f89ac07a949bd32bf9363aae&mc=true&n=pt14.1.25&r=PART&ty=HTML#se14.1.25_1103
- [11] D. Thurston, “Amphibious Aircraft Design”, Business Aircraft Meeting, Wichita, KS, April 2-5, 1974.
- [12] W. Diehl, “Static Stability of Seaplane Floats and Hulls”, Technical notes, Bureau of Aeronautics, U.S.N, NACA, March, 1924.
- [13] K. Wood, “Aerospace Vehicle Design, 3rd edition”, Johnson Pub. Co, Boulder, Colorado, 1968.
- [14] D. Allen, W. Haisler, “Introduction to Aerospace Structural Analysis”, Wiley, New York, 1985.
- [15] T.H.G. Megson, “Aircraft Structures for Engineering Students, 4th edition”, Butterworth-Heinemann, Oxford, 2007.
- [16] R. Nelson, “Flight Stability and Automatic Control, 2nd edition”, WCB/McGraw Hill, Boston, Ma, 1998.
- [17] B. Stevens, “Aircraft control and Simulation, 2nd edition”, Wiley, Hoboken, NJ, 2003.
- [18] J. Roskam, “Airplane flight Dynamics and automatic flight controls”, Roskam Aviation and Engineering Corp, Lawrence, Kansas, 1979.
- [19] Goodyear Aircraft Tire DataBook, https://www.goodyearaviation.com/resources/pdf/databook_7_2016.pdf
- [20] L Mehl, A. Parson, “Aircraft Anti-Icing Systems”, presentation, Virginia Tech, http://www.dept.aoe.vt.edu/~mason/Mason_f/AntilcingT4.ppt.
- [21] "Beechcraft 1900D: Fuel, Emissions & Cost Savings Operational Analysis". Specific Range Solutions Ltd. February 21, 2012.
- [22] "Dornier 228 Advanced Commuter Brochure". RUAG.

[23] Vikingair Twin-Otter Operating Cost Estimates Calculator,
http://www.vikingair.com/buying-twin-otter/operating-cost-calculator/estimates?operating_empty_weight=7915&number_of_crew=2&reserve_fuel=45&route_distance=300&max_takeoff_weight=12500&fuel_cost=5.2&labor_rate=1&submit=See+Results